The Astrophysical Journal, 975:113 (22pp), 2024 November 1 https://doi.org/10.3847/1538-4357/ad793f

Learning the Universe: GalactISM Simulations of Resolved Star Formation and Galactic Outflows across Main-sequence and Quenched Galactic Environments

Sarah M. R. Jeffreson[1], Eve C. Ostriker[2,3], Chang-Goo Kim[2], Jindra Gensior[4], Greg L. Bryan[5,6], Timothy A. Davis[7], Lars Hernquist[1], and Sultan Hassan[6,8,9,10]
[1] Center for Astrophysics, Harvard & Smithsonian, 60 Garden Street, Cambridge, MA 02138, USA; sarah.jeffreson@cfa.harvard.edu
[2] Department of Astrophysical Sciences, Princeton University, 4 Ivy Lane, Princeton, NJ 08544, USA
[3] Institute for Advanced Study, 1 Einstein Drive, Princeton, NJ 08540, USA
[4] Department of Astrophysics, University of Zurich, Winterthurerstrasse 190, 8057 Zurich, Switzerland
[5] Department of Astronomy, Columbia University, 550 W. 120th Street, New York, NY 10027, USA
[6] Center for Computational Astrophysics, Flatiron Institute, 162 5th Avenue, New York, NY 10010, USA
[7] Cardiff Hub for Astrophysics Research & Technology, School of Physics & Astronomy, Cardiff University, Cardiff, CF24 3AA, UK
[8] Center for Cosmology and Particle Physics, Department of Physics, New York University, 726 Broadway, New York, NY 10003, USA
[9] Department of Physics & Astronomy, University of the Western Cape, Cape Town 7535, South Africa
Received 2024 April 26; revised 2024 September 4; accepted 2024 September 8; published 2024 October 29

Abstract

We present a suite of six high-resolution chemodynamical simulations of isolated galaxies, spanning observed disk-dominated environments on the star-forming main sequence, as well as quenched, bulge-dominated environments. We compare and contrast the physics driving star formation and stellar feedback among the galaxies, with a view to modeling these processes in cosmological simulations. We find that the mass loading of galactic outflows is coupled to the clustering of supernova explosions, which varies strongly with the rate of galactic rotation $\Omega = v_{\rm circ}/R$ via the Toomre length, leading to smoother gas disks in the bulge-dominated galaxies. This sets an equation of state in the star-forming gas that also varies strongly with Ω, so that the bulge-dominated galaxies have higher midplane densities, lower velocity dispersions, and higher molecular gas fractions than their main-sequence counterparts. The star formation rate in five out of six galaxies is independent of Ω and is consistent with regulation by the midplane gas pressure alone. In the sixth galaxy, which has the most centrally concentrated bulge and thus the highest Ω, we reproduce dynamical suppression of the star formation efficiency in agreement with observations. This produces a transition away from pressure-regulated star formation.

Unified Astronomy Thesaurus concepts: Disk galaxies (391); Lenticular galaxies (915); Spiral galaxies (1560); Interstellar medium (847); Star formation (1569); Hydrodynamical simulations (767); Stellar feedback (1602); Galactic and extragalactic astronomy (563); Galaxy processes (614); Galaxy properties (615); Galaxy structure (622)

1. Introduction

Since the first detections of cold gas in elliptical, early-type galaxies (ETGs) at low redshift (T. Wiklind & G. Rydbeck 1986; T. G. Phillips et al. 1987), the presence of star-forming gas in such galaxies has been shown to be relatively common. Molecular gas has been detected in at least 22% of local ETGs (G. A. Welch & L. J. Sage 2003; F. Combes et al. 2007; L. M. Young et al. 2011; T. A. Davis et al. 2019), and some of the most massive ETGs are found to have large molecular gas reservoirs between 10^9 and 10^{11} solar masses (e.g., P. Salomé & F. Combes 2003; H. R. Russell et al. 2016; E. O'Sullivan et al. 2018; H. R. Russell et al. 2019).

With the recent advent of high-sensitivity submillimeter interferometers, it has become possible to resolve these molecular gas reservoirs in great detail, and even to distinguish individual giant molecular clouds (GMCs) within them (D. Utomo et al. 2015; L. Liu et al. 2021; T. G. Williams et al. 2023; A. Lu et al. 2024). Such studies demonstrate that the interstellar media (ISMs) of lenticular and elliptical galaxies display very different properties from their main-sequence spiral galaxy counterparts, forming very smooth gas disks that more closely resemble protoplanetary disks than they do galaxies (T. A. Davis et al. 2022). A large fraction of these ETGs also display cold gas and molecular gas depletion times that are elevated by up to an order of magnitude, relative to the values measured in main-sequence galaxies. Interestingly, these prolonged depletion times are not seen in all ETGs: the average increase in the cold gas depletion time across the population of observed ellipticals, relative to spiral galaxies, is just 2.5 times (T. A. Davis et al. 2014).

This suppression of star formation in the cold gas of bulge-dominated galaxies is also a prominent feature in large galaxy surveys that directly detect atomic and molecular gas over a range of redshifts (e.g., A. Saintonge et al. 2012; L. J. Tacconi et al. 2018; D. Colombo et al. 2020). Computing gas masses via the dust reddening of optical spectra in the Sloan Digital Sky Survey (SDSS) sample, J. M. Piotrowska et al. (2022) have shown a suppression of the molecular gas star formation efficiency (SFE) in quenched galaxies by two orders of magnitude, comparable to the reduction factor in their overall gas fractions. Across the EDGE-CALIFA survey (D. Colombo et al. 2020), it is found that the offset from the galactic star-forming main sequence for low gas fraction galaxies is driven predominantly by a large drop in their SFEs per unit molecular

[10] NHFP Hubble fellow.

gas mass, rather than by variation in the molecular gas fractions.

Such data indicate that the quenching of star formation occurs as a result of both the removal of star-forming gas from galaxies and the quenching of star formation within the remaining cold gas. While feedback from active galactic nuclei (AGNs) has been shown to effectively eject gas from galaxies and to halt the accretion of new gas by heating the surrounding intracluster medium (see A. C. Fabian 2012, and references therein), it has not been shown to suppress star formation within the remaining cold gas. A mechanism shown to produce the latter effect in numerical simulations is "dynamical suppression" (M. Martig et al. 2009, 2013; J. Gensior et al. 2020; J. Gensior & J. M. D. Kruijssen 2021), whereby stabilizing torques due to the rapid rate of galactic rotation in bulge-dominated environments prevents the collapse of cold gas, and thus the formation of new stars.

To correctly predict and therefore understand the pathways to the quenching of star formation throughout the course of galaxy evolution, it is therefore necessary to correctly model the physics driving star formation and stellar feedback in the cold ISMs of both star-forming and quenched galaxies. Unfortunately, state-of-the-art hydrodynamical cosmological volume simulations lack the resolution to model this cold, star-forming ISM. Though substantial work has been done to model resolved star formation via cosmological zoom-in simulations (e.g., O. Agertz et al. 2013; J. Chen et al. 2016; R. J. J. Grand et al. 2017; P. F. Hopkins et al. 2018), it is currently infeasible to extend such models to volumes containing many thousands of galaxies.

Currently, cosmological volume simulations adopt subgrid treatments for star formation, stellar feedback, and galactic winds that are typically calibrated to observed scalings in low-redshift, main-sequence galaxies (in the case of star formation and stellar feedback) or that are tuned to reproduce key galaxy scaling relations (in the case of wind mass and energy loading; see M. C. Smith et al. 2024 and references therein). In particular, the depletion time is commonly calibrated to the relationship between the star formation rate (SFR) and gas density in nearby spiral galaxies (e.g., V. Springel & L. Hernquist 2003), the same relationship that is shifted systematically for the ISMs of ETGs.

Perhaps as a result of these highly simplified subgrid models, hydrodynamical cosmological simulations are currently unable to accurately model the onset of star formation quenching as a function of stellar mass M_*, black hole mass $M_{\rm BH}$, and halo mass $M_{\rm Halo}$ (D. Nelson et al. 2018; J. M. Piotrowska et al. 2022). Of the Illustris (M. Vogelsberger et al. 2014), IllustrisTNG (D. Nelson et al. 2018), and EAGLE (J. Schaye et al. 2015) simulations, J. M. Piotrowska et al. (2022) find that IllustrisTNG displays the best qualitative agreement with trends in the SDSS at low redshift but overestimates the mass at which quenching sets in, by three times in M_* and around 10 times in $M_{\rm Halo}$ and $M_{\rm BH}$. The discrepancy in the quenched fraction of galaxies with M_* is also reproduced by D. Nelson et al. (2018) and M. Donnari et al. (2019), though we note that the comparison between simulations and observations may be affected by sample selection, the choice of SFR indicator, and a host of other complicating factors (M. Donnari et al. 2021).

One of the key goals of the Learning the Universe Simons Collaboration (and one of its predecessors, the SMAUG collaboration) is to substitute the existing, empirically calibrated or tuned subgrid prescriptions in cosmological simulations with models that are calibrated based on higher-resolution simulations, which capture the relevant physics on smaller scales. The collaboration therefore aims to produce cosmological simulations that no longer require empirical calibration or tuning, allowing for the predictive modeling of star formation quenching, among other physics. In this paper, we introduce the first six of the "GalactISM" simulations: a suite of high-resolution chemodynamical isolated galaxy simulations spanning observed, dynamically diverse star-forming environments from the galactic star-forming main sequence of spiral galaxies to the population of fast-rotating quenched[11] ETGs at low redshift. We examine the SFR, the SFE, and the properties of galactic outflows across these environments, as a function of large-scale galaxy properties such as the midplane pressure, density, and rotation rate. We therefore determine which subgrid processes can be modeled by physically motivated analytic theory in the form of power-law relationships, and determine the galactic environments in which nonlinear deviations from these power-law relationships arise. Such nonlinear deviations might in the future be accounted for by statistical or learned modeling techniques—another facet of the Learning the Universe collaboration.

The GalactISM simulations are complementary to the "TIGRESS" (C.-G. Kim & E. C. Ostriker 2017; C.-G. Kim et al. 2020) and "TIGRESS-NCR" (C.-G. Kim et al. 2023a; J.-G. Kim et al. 2023b) frameworks—magnetohydrodynamic (MHD) simulations using ATHENA (J. M. Stone et al. 2008; J. M. Stone & T. Gardiner 2009), with star formation and supernova+radiation feedback that have the same (2–4 pc) resolution in all ISM phases, including the low-density, hot gas.[12] The latter allows for full UV radiative transfer via adaptive ray-tracing, as well as photochemistry (J.-G. Kim et al. 2023b). By contrast, the GalactISM simulations employ adaptive refinement in the moving-mesh code AREPO and use the mechanical supernova and H II region feedback prescriptions based on momentum injection introduced in S. M. R. Jeffreson et al. (2021), appropriate when it is not possible to fully resolve the Sedov–Taylor blast waves and Strömgren spheres. At the lower resolution of GalactISM (corresponding to ∼1–10 pc in the molecular gas and ∼30–60 pc in the warm gas) we can model entire galaxies and the HCO chemistry of their three-phase, star-forming gas reservoirs relatively efficiently, allowing for the potential influence of inward radial mass transport (e.g., M. Krumholz & A. Burkert 2010; N. J. Goldbaum et al. 2015; M. R. Krumholz et al. 2018) and for the later inclusion of a circumgalactic medium, necessary for the modeling of high gas fraction, high-redshift galactic environments. We also produce a statistical sample of around 60,000 GMCs across these six simulations.

The remainder of the paper is structured as follows: In Section 2 we introduce the GalactISM simulation suite, along with the numerical models used for star formation, stellar feedback, chemistry, and cooling. In Section 3 we give an overview of the dynamical properties, gas-phase distribution and morphology, and star-forming behavior of our galaxies, in comparison to observed ETGs from the ATLAS^{3D} survey

[11] We use the term "quenched" to denote galaxies with an sSFR $\leqslant 1 \times 10^{-11}\,{\rm yr}^{-1}$.

[12] This higher resolution in the hot gas phase makes it possible to follow the Sedov–Taylor (energy-conserving, momentum-generating) stage of supernova remnant (SNR) evolution, in which hot gas is created in shocks, and the resolved interaction of expanding SNRs with the warm/cold gas phases, to drive turbulence on a range of scales.

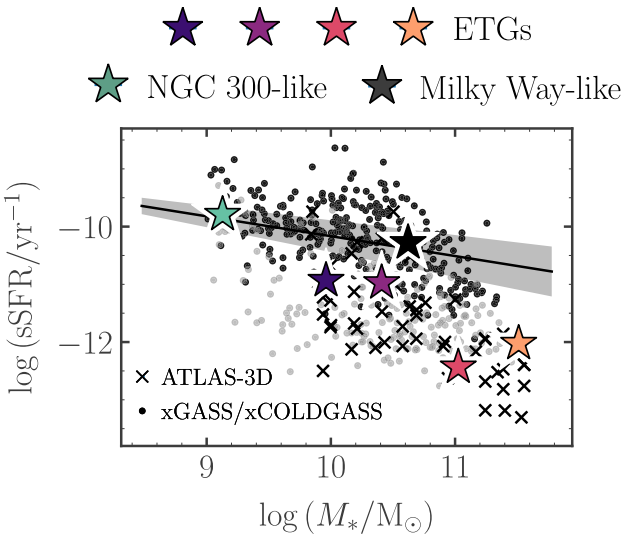

Figure 1. Each of the six isolated galaxy simulations (stars) in the plane of total stellar mass M_* vs. sSFR. Black data points represent atomic and molecular gas detections, respectively, from the xGASS (B. Catinella et al. 2018) and xCOLDGASS (A. Saintonge et al. 2017) surveys, while gray data points represent nondetections. Black crosses represent data from the ATLAS^{3D} survey (M. Cappellari et al. 2011). The galactic star-forming main sequence as defined in B. Catinella et al. (2018) is given by the black solid line and shaded region.

(M. Cappellari et al. 2011). Section 4 provides a systematic analysis of the properties of stellar-feedback-driven galactic outflows in our simulation and their dependence on the level of supernova clustering and gravitational stability in the simulated gas disks. The scaling of the SFR surface density with the gas surface density, the midplane pressure, and the ISM weight are investigated in Section 5, along with the equation of state (EOS) between the gas density and pressure. Finally, we conclude with a discussion and summary of our results in Section 6.

2. Simulation Suite

The six chemodynamical isolated galaxy simulations presented in this work consist of one large spiral (Milky Way–like) galaxy, one dwarf spiral (NGC 300–like) galaxy, and four ETGs. The physical properties of the ETG simulations are matched to the observations of elliptical galaxies from the ATLAS^{3D} and MASSIVE surveys. Together, the simulated galaxies span over two orders of magnitude in total stellar mass and specific SFR (sSFR; see Figure 1), from the galactic star-forming main sequence (black line) down to the quenched galaxy population below.

2.1. Initial Conditions

We generate initial conditions for our early-type and NGC 300–like galaxy simulations using the MAKENEWDISK code (V. Springel et al. 2005). The physical properties of the dark matter halos, stellar disks and bulges, and gas disks for each simulation are shown in Table 1, along with the mass resolutions of the associated dark matter particles, stellar particles, and gas cells. For the Milky Way–like simulation, we use the AGORA initial condition (J.-h. Kim et al. 2014), which is designed to resemble a Milky Way–like galaxy at redshift $z = 0$. All six dark matter halos are of Navarro–Frenk–White (NFW; J. F. Navarro et al. 1997) type, and our stellar and gas disks follow an exponential form. The stellar bulge follows an H. C. Plummer (1911) profile in the ETG initial conditions and an L. Hernquist (1990) profile in the Milky Way–like initial condition. None of our initial conditions contain a hot halo / circumgalactic medium component, consistent with the AGORA initial condition. Our median gas cell mass is 859 $M_\odot$ for all galaxies.

We note that the properties of the simulated gas and stellar disks change substantially between the beginning of the simulation (0 Myr) and the first simulation time analyzed ($t_{\rm start}$), as the gas disk settles into a state of dynamical equilibrium. Unless otherwise stated, Table 1 therefore gives the median value of each disk parameter during the period of simulation times analyzed, during which the values do not change substantially.

2.1.1. Early-type Galaxies

The physical parameters for our ETG initial conditions are designed to span the observable properties of ETGs from the MASSIVE (C.-P. Ma et al. 2014) and ATLAS^{3D} (M. Cappellari et al. 2011) surveys (transparent data points in Figure 2). We match the observed variation of the halo mass (M_{200}; top left), stellar half-light radius ($R_{*,1/2}$; top right), gas fraction (bottom left), extent of the CO-luminous molecular gas disk ($R_{\rm CO}$; bottom middle), and surface density of the CO-luminous molecular gas disk ($\Sigma_{\rm gas}(R < R_{\rm CO})$; bottom right), as a function of the total stellar mass M_* (x-axis of each panel). The black lines represent the observed median values at each stellar mass, while the circled bars represent the simulated values. The vertical extent of each bar represents the variation in value across the simulation times analyzed. The stellar masses of our galaxies span the observed samples in logarithmic intervals: our four ETGs have stellar masses of $M_* = 10^{10}$, $10^{10.5}$, 10^{11}, and $10^{11.5}\,M_\odot$.

The disk-to-bulge mass ratios of our simulated galaxies are set to $M_{*,\rm disk}/M_{*,\rm bulge} = 0.2$, which will allow us, in the future, to compare our simulated molecular cloud samples to resolved observations of molecular gas in the lenticular galaxies studied by D. Utomo et al. (2015), L. Liu et al. (2021), and T. G. Williams et al. (2023).

According to the observable parameters presented in Figure 2, we constrain the remaining physical properties of our ETG initial conditions as follows. First, we determine the concentration parameters c of our dark matter halos according to the halo concentration–mass relation of A. A. Dutton & A. V. Macciò (2014), for NFW fits to N-body halo density profiles in the cosmology of the Planck satellite (their Equation (8)). We use spin parameters of $\lambda = 0.04$ across our simulation suite, in accordance with the empirically derived values of X. Hernandez et al. (2007), across an SDSS sample of spiral and elliptical galaxies.

Within MAKENEWDISK, the stellar disk scale length is set according to its angular momentum, which is in turn determined by the spin of the dark matter halo (see Section 2.2.1 of V. Springel et al. 2005, and references therein). We then set the stellar bulge scale length such that the observed value of $R_{*,1/2}$ is retrieved at each stellar mass, disk-to-bulge ratio, and gas fraction. Finally, we set the gas disk scale length to match the sizes $R_{\rm CO}$ and surface densities $\Sigma_{\rm gas}(R < R_{\rm CO})$ of the observed molecular gas disks at each stellar mass. The CO-luminous gas fraction is computed for each simulation output using the DESPOTIC astrochemistry and radiative transfer model (M. R. Krumholz 2013, 2014), as described in Appendix A.

Table 1
Physical Properties of the Initial Conditions for Each Galaxy Simulation, Along with the Simulation Times between Which the Simulation Outputs Are Analyzed, t_{start} and t_{end}

Property	Symbol	ETGs				Milky Way	NGC 300
Analysis start (Myr)	t_{start}	100	100	100	100	300	500
Analysis end (Myr)	t_{end}	400	400	400	400	600	800
Total stellar mass	$M_*/M_\odot$	10^{10}	$10^{10.5}$	10^{11}	$10^{11.5}$	4.734×10^{10}	1×10^9
Stellar disk mass	$M_{*,\,d}/M_\odot$	2×10^9	6.3×10^9	2×10^{10}	6.3×10^{10}	4.297×10^{10}	1×10^9
Stellar bulge mass	$M_{*,\,b}/M_\odot$	8×10^9	2.5×10^{10}	8×10^{10}	2.5×10^{11}	3.437×10^9	0
Gas fraction (0 Myr)	M_{gas}/M_*	0.016	0.016	0.0016	0.0016	0.18	0.68
Gas fraction (t_{start})	M_{gas}/M_*	0.012	0.011	0.0015	0.0012	0.12	0.57
Bulge-to-disk ratio	$M_{*,\,b}/M_{*,\,d}$	4	4	4	4	0.125	0
Concentration parameter	c	8.6	7.4	6.7	6.4	10	15.4
Virial velocity	V_{200}/km s^{-1}	130	200	280	370	150	63
Spin parameter	λ	0.04	0.04	0.04	0.04	0.04	0.04
Stellar disk scale radius	$R_{*,\,d}$/kpc	3.96	6.67	9.64	13.5	3.43	1.39
Stellar bulge scale radius	$R_{*,\,b}$/kpc	1.35	1.85	2.8	8.75	0.34	-
Gas disk scale radius	R_{gas}/kpc	0.30	0.47	0.37	0.62	3.43	3.44
Stellar disk scale height	$h_{*,\,d}$/pc	50	49	47	45	123	90
Gas disk scale height	h_{gas}/pc	30	25	20	30	82	110
Gas cell resolution	$\epsilon_{gas}/M_\odot$	859	859	859	859	859	859
Stellar particle resolution	$\epsilon_*/M_\odot$	5×10^3	5×10^3	5×10^3	5×10^3	5×10^3	5×10^3
Dark matter particle resolution	$\epsilon_{halo}/M_\odot$	1.25×10^5	1.25×10^5	1.25×10^5	1.25×10^5	1.25×10^5	1.25×10^5

Note. Unless otherwise stated, all values are median values between t_{start} and t_{end}.

The stellar disk scale height in our initial condition is set iteratively by MAKENEWDISK, such that the stellar disk achieves a state of hydrostatic equilibrium within the full three-dimensional potential of the galaxy, assuming the density profile of a uniform isothermal sheet. The three-dimensional velocity structures of the collisionless dark matter and stellar components are set according to the triaxial approximation outlined in Section 2.3 of V. Springel et al. (2005), and we initialize the gas scale height to 1/10 of the stellar value, with a temperature of 10^4 K. However, once the simulation begins, the gas and stellar disk scale heights self-adjust to smaller values as the disks evolve toward a state of dynamical equilibrium under the influence of stellar feedback. Therefore, Table 1 gives the median values for the stellar and gas disk scale heights over the simulation period analyzed in this work. These values are stable once the disk has reached a state of dynamical equilibrium at t_{start}.

2.1.2. Milky Way–like Galaxy

The AGORA disk initial condition (J.-h. Kim et al. 2014) is designed to resemble a Milky Way–like galaxy at redshift $z \sim 0$. It has a dark matter halo mass of $M_{200} = 1.07 \times 10^{12}\,M_\odot$, a virial radius of $R_{200} = 205$ kpc, a halo concentration of $c = 10$, and a spin parameter of $\lambda = 0.04$. The stellar bulge has a mass of $3.437 \times 10^9\,M_\odot$, while the exponential disk has a mass of $4.297 \times 10^{10}\,M_\odot$, a scale length of 3.43 kpc, and an initial scale height of 343 pc.

The stellar disk scale height equilibrates to a value of 123 pc over the first 300 Myr of the simulation run time, and the total gas disk scale height equilibrates to a value of 82 pc. Specifically, the final molecular disk scale height is around 50 pc, the atomic disk scale height is around 200 pc, and the ionized gas extends to distances of >1 kpc above the midplane. We acknowledge that while these multiphase gas disk scale heights are in reasonable agreement with edge-on observations of external galaxies, the stellar disk scale height is smaller than expected. The initial stellar velocity dispersion was chosen to be consistent with J.-h. Kim et al. (2014), but a larger initial vertical velocity dispersion would have resulted in a thicker equilibrium stellar disk. The bulge-to-stellar-disk ratio is 0.125, and the initial gas fraction is 0.18.

2.1.3. NGC 300–like Galaxy

For our NGC 300–like simulation, we match the structural parameters of the dark matter halo, stellar disk, and gas disk from T. Westmeier et al. (2011). The dark matter halo has a circular velocity of $V_{200} = 76$ km s^{-1} at the virial radius, corresponding to a virial mass of $M_{200} = 8.3 \times 10^{10}\,M_\odot$. We set an NFW concentration parameter of 15.4, which gives a reasonable approximation to the observed rotation curve of the baryons in NGC 300, and choose a spin parameter of $\lambda = 0.04$, as explained in Section 2.1.1. The stellar disk has a mass of $1 \times 10^9\,M_\odot$ and an initial scale height of 0.28 kpc, while the gas disk has a mass of $2 \times 10^9\,M_\odot$ and an isothermal temperature of 10^4 K. Similarly to the ETG initial conditions, the stellar disk scale length, along with the initial velocity structure of the collisionless particles and gas cells, is set according to the methods outlined in V. Springel et al. (2005). The stellar disk scale height equilibrates to a value of 90 pc over the first 500 Myr of the simulation run time, and the gas disk scale height equilibrates to a value of 110 pc.

2.2. Galactic Rotation Curves

In Figure 3 we show the midplane circular velocity v_{circ} of each simulated galaxy as a function of galactocentric radius R

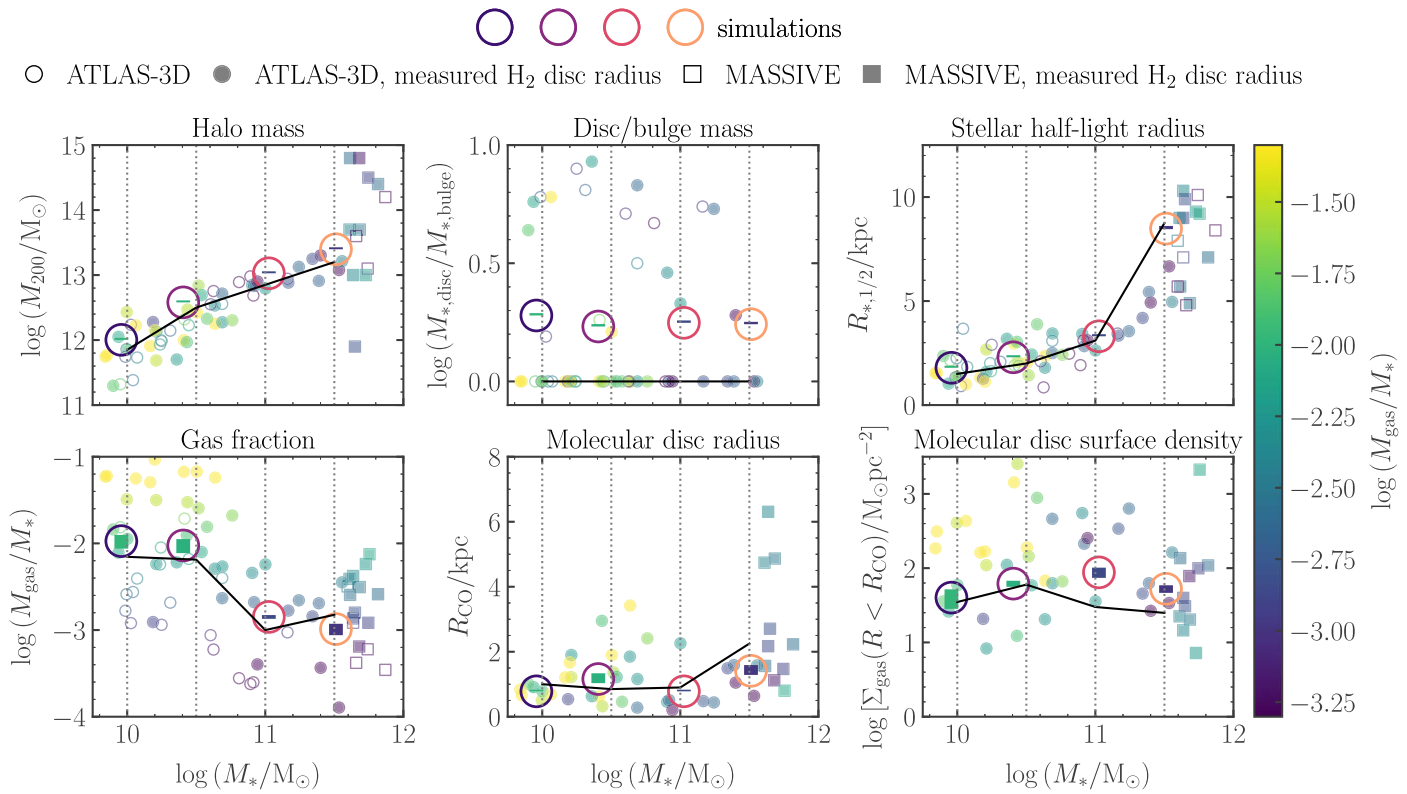

Figure 2. Physical properties of the simulated ETGs (circled bars), compared to observed galaxies from the ATLAS^{3D} (circular transparent data points) and MASSIVE (square transparent data points) galaxy surveys. Open data points represent observed galaxies with no measured values of the molecular gas disk size R_{CO} (bottom middle panel), and so no measured values of the molecular gas surface density $\Sigma_{H_2,\,CO}$ (bottom right panel). Black lines represent the median observed values of each physical quantity in stellar mass bins centered on $M_* = 10^{10}$, $10^{10.5}$, 10^{11}, and $10^{11.5}\,M_\odot$. The vertical extent of the circled bars represents the values spanned by the simulated galaxies between the simulation times of 100 and 400 Myr, colored according to their gas fractions. Our simulations roughly reproduce these median values (see Section 2.1). Observational references: M. Cappellari et al. (2011), D. Krajnović et al. (2013), M. Cappellari et al. (2013), and T. A. Davis et al. (2013, 2014) for ATLAS^{3D}, and M. Veale et al. (2018), T. A. Davis et al. (2019), and T. Davis (2024, private communication) for MASSIVE.

(first row of panels, thick transparent lines). We also show the epicyclic frequency κ (second row, thick transparent lines), which is given by $\kappa = \Omega\sqrt{2(1+\beta)}$ for an angular velocity of Ω and a shear parameter $\beta = d\ln v_{circ}/\ln R$. For both v_{circ} and κ, we show the separate components that are contributed by the gravitational potential Φ_{gas} due to the gas particles in the simulation, Φ_{DM} due to the dark matter particles, $\Phi_{*,disk}$ due to the stellar disk, and $\Phi_{*,bulge}$ due to the stellar bulge. In the bottom panels, we directly compare the values of v_{circ} and κ across the entire simulation suite.

The rotation speed is largest ($\sim$300 km s^{-1}) in the ETG of stellar mass $M_* = 10^{11}\,M_\odot$, due to the higher concentration of its stellar bulge. While this galaxy does not have the largest stellar mass, this mass is concentrated within the smallest stellar half-light radius $R_{*,1/2}$. Its higher bulge concentration can be quantified by its central stellar surface density $\mu_* = 1700\,M_\odot\,pc^{-2}$, 70% higher than the second most compact bulge, with $\mu_* = 1000\,M_\odot\,pc^{-2}$. The value of μ_* is measured within $R_{*,1/2}$ for each galaxy and listed above the top row of panels in Figure 3.

We see that the values of μ_* and the speed of galactic rotation are approximately correlated across our simulation suite: as such, the central stellar surface density can be used as a proxy for the value of κ (and thus the degree of support provided to the gas by tidal, centrifugal, and Coriolis forces) in a given galaxy. The elevated bulge-induced rate of rotation in the $M_* = 10^{11}\,M_\odot$ ETG is an important feature of this simulation, to which we will later return.

By contrast to the ETGs, the Milky Way–like and NGC 300–like galaxies (right panels) have much lower levels of rotation-induced shear outside the central kiloparsec. Their rotation curves are dominated by their dark matter and stellar/gas disk components, with negligible or zero contribution to the circular velocity from a stellar bulge component. The galactic center region of the Milky Way–like galaxy (black lines, bottom panels) is the most strongly rotationally supported[13] region of the disk galaxies and matches the value of κ in only the most weakly supported ETG (dark-purple lines, bottom panels).

We note that the circular velocity of the NGC 300–like galaxy (green lines, bottom panels) is around 25% higher than the value observed by T. Westmeier et al. (2011), which varies from 50 to 80 km s^{-1} between galactocentric radii of 0.3 and 6 kpc, while ours has an average value of 100 km s^{-1}. Our simulated value is more typical of other dwarf spiral galaxies, such as M33 (e.g., E. W. Koch et al. 2018).

2.3. Hydrodynamics, Chemistry, Star Formation, and Feedback

The initial conditions described in Section 2.1 are evolved using the moving-mesh hydrodynamics code AREPO (V. Springel 2010). In particular, the gas reservoir is modeled using an

[13] Throughout this paper, we use the term "rotational support" to refer to the degree of support against gravitational collapse that is provided to the gas in a galaxy by the tidal, centrifugal, and Coriolis forces. This support depends on both the magnitude and gradient of the gas circular velocity v_{circ}, and thus on the gravitational potential of the galaxy.

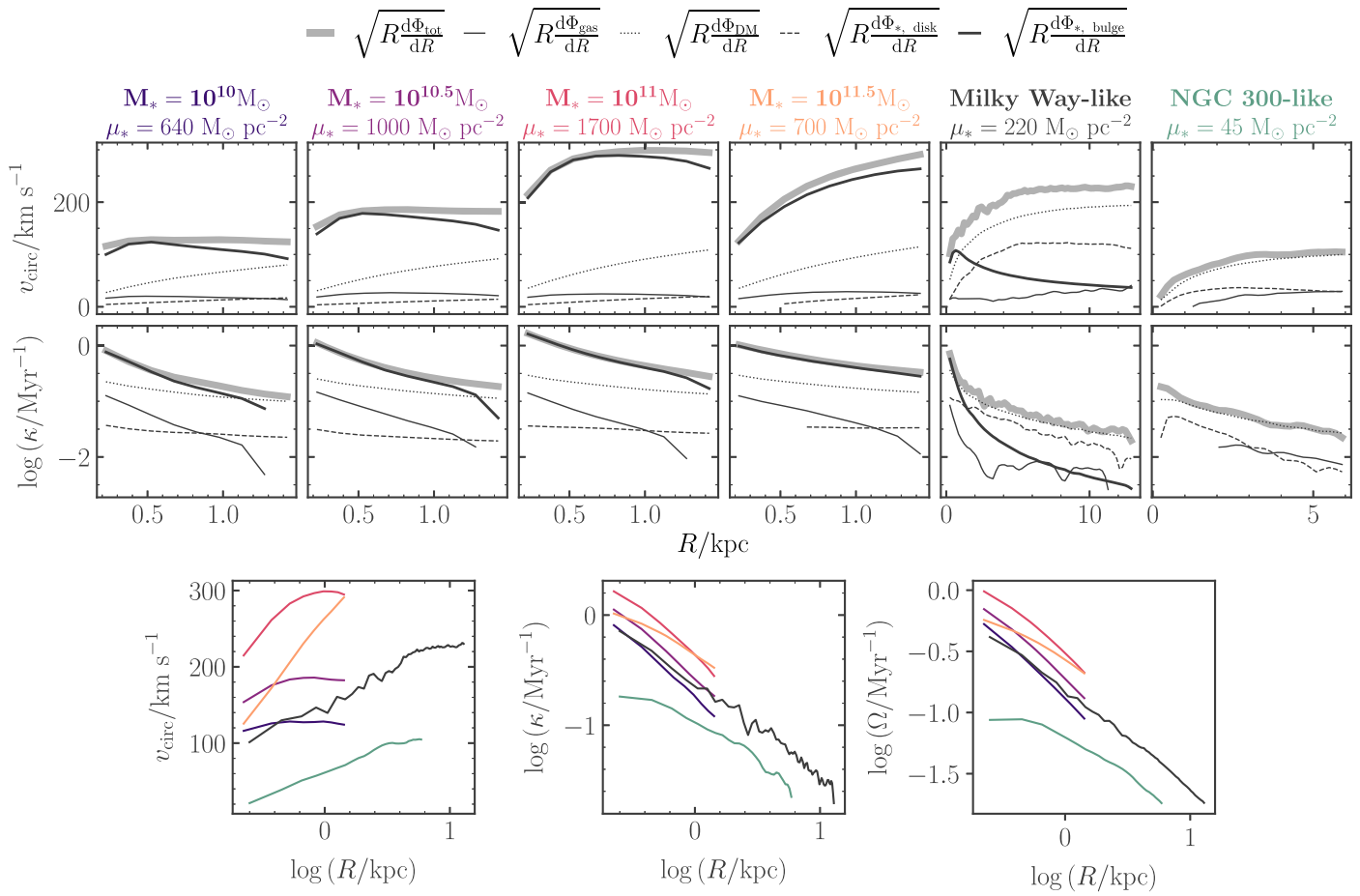

Figure 3. Top: midplane circular velocity v_{circ} and epicyclic frequency κ (thick transparent lines) as a function of galactocentric radius R for each of the simulated galaxies across the radial extent of the gas disk, computed directly from the gravitational potential exerted by the gas (thin lines), dark matter (dotted lines), disk stars (dashed lines), and bulge stars (thick lines). Note that the ETG gas disks are much smaller than those of the main-sequence galaxies. The central stellar surface density μ_* is given below the stellar mass at the top of each column. Galactic rotation in the ETGs is dominated by the stellar bulge component. Each rotation profile is computed at one simulation time only, but the values change negligibly over the time period analyzed for each simulation. Bottom: comparison of the total circular velocities and epicyclic frequencies for each of the six galaxy simulations.

unstructured moving mesh that is defined by a Voronoi tesselation about a discrete set of points, moving with the local gas velocity. A hybrid TreePM gravity solver is used to calculate the gravitational acceleration vectors of the Voronoi gas cells, stellar particles, and dark matter particles. We employ the native adaptive gravitational softening scheme for the gas cells, with a minimum softening length of 3 pc and a gradation of 1.5 times the Voronoi gas cell diameter. We set the softening length of the star particles to a constant value of 3 pc and set the softening length of the dark matter particles to 280 pc, according to the convergence tests presented in C. Power et al. (2003).

Our models for the temperature and chemical composition of the gas in our simulations, along with the rate of star formation in this gas and the rate of energy and momentum injection due to stellar feedback, are identical to those described in S. M. R. Jeffreson et al. (2024). We give a brief overview of these models below, but we refer the reader to the cited works for further details.

We use the nonequilibrium network for hydrogen, carbon, and oxygen chemistry described in R. P. Nelson & W. D. Langer (1997) and in S. C. O. Glover & M.-M. Mac Low (2007b, 2007a), coupled to the atomic and molecular cooling function of S. C. O. Glover et al. (2010). This includes cooling due to fine-structure emission from C^+, O, and Si^+; Lyα emission from atomic hydrogen; H_2 line emission, gas-grain cooling; and electron recombination on grain surfaces and in reaction with polycyclic aromatic hydrocarbons (PAHs). In hot gas, the chemical network additionally allows for cooling via the collisional processes of H_2 dissociation, bremsstrahlung, and the ionization of atomic hydrogen. The dominant heating mechanism is photoelectric emission from dust grains and PAHs, with lesser contributions from cosmic-ray ionization and H_2 photodissociation by the UV interstellar radiation field (ISRF). We assign a value of 1.7 Habing (H. J. Habing 1968) units for the ISRF strength according to J. S. Mathis et al. (1983) and a value of $2 \times 10^{-16}\,s^{-1}$ to the cosmic-ray ionization rate (e.g., N. Indriolo & B. J. McCall 2012).[14] The dust grain number density is computed by assuming the solar value for the dust-to-gas ratio, and the dust temperature is obtained according to the procedure described in Appendix A of S. C. O. Glover & P. C. Clark (2012). Finally, we use the TREECOL algorithm presented in P. C. Clark et al. (2012) to model the dust shielding and self-shielding of molecular

[14] These choices are based on the solar neighborhood; more realistically, these values would vary in time proportional to the local SFR per unit area. A lower (higher) radiation field will tend to enhance (decrease) the cold-to-warm gas mass ratio and to decrease (increase) the thermal pressure.

hydrogen from dissociation by the ISRF, allowing us to track the nonequilibrium abundance of molecular hydrogen during the run time of the simulation.

The SFR volume density in our simulation is given by

$$\frac{d\rho_{*,i}}{dt} = \frac{\epsilon_{\rm ff}\,\rho_i}{t_{{\rm ff},i}},\ \ \rho_i \geqslant \rho_{\rm thresh},\ T_i \leqslant T_{\rm thresh} \tag{1}$$

$$\frac{d\rho_{*,i}}{dt} = 0,\ \ \rho_i < \rho_{\rm thresh},\ T_i > T_{\rm thresh}, \tag{2}$$

where $t_{{\rm ff},i} = \sqrt{3\pi/(32G\rho_i)}$ is the local freefall timescale for the gas cell i with a mass volume density of ρ_i, and $\epsilon_{\rm ff}$ is the SFE per freefall time, which follows the parameterization of P. Padoan et al. (2017), such that

$$\epsilon_{\rm ff} = 0.4\exp(-1.6\alpha_{\rm vir}^{0.5}). \tag{3}$$

The virial parameter $\alpha_{\rm vir}$ on cloud scales is computed during the simulation run time within overdense regions surrounding each star-forming gas cell; the scale of each overdensity is determined via a variant of the V. V. Sobolev (1960) approximation, as the characteristic length scale $L = \rho/|\nabla\rho|$ for changes in the density of the surrounding gas, where $\nabla\rho = \partial\rho/\partial r$ is the density gradient with distance r from the central gas cell. The algorithm is described in detail in J. Gensior et al. (2020). The median radius of these overdensities is $\sim$10 pc across our simulation suite, and the average number of gas cells within each overdensity is 140. We set an upper limit of $T_{\rm thresh} = 100$ K on the temperature below which star formation is allowed to occur and a lower limit of $\rho_{\rm thresh}/m_{\rm H}\mu = 100\,{\rm cm}^{-3}$ on the density, where μ is the mean mass per H atom.

The star particles formed via Equations (1) and (3) generate energy and momentum from supernova explosions and presupernova H II regions, via the stellar feedback prescription described in S. M. R. Jeffreson et al. (2021). To compute the number of supernovae, ejected mass, and photoionizing luminosity of each star particle, we assign a stellar population drawn stochastically from a G. Chabrier (2003) initial stellar mass function, using the Stochastically Lighting Up Galaxies (SLUG) stellar population synthesis model (R. L. da Silva et al. 2014; M. R. Krumholz et al. 2015). An energy of 10^{51} erg per supernova is assumed, and the terminal momentum from these supernovae is explicitly calculated using the few-supernovae parameterization derived from the high-resolution simulations of E. S. Gentry et al. (2017, their Equation (17)). This kinetic energy, along with the remaining thermal energy, is injected into all gas cells surrounding each star particle.

The photoionizing luminosity associated with H II regions is converted to a momentum per unit time via the model of S. M. R. Jeffreson et al. (2021), following the analytic work of C. D. Matzner (2002) and M. R. Krumholz & C. D. Matzner (2009) to account for both radiation pressure and the momentum injected via the "rocket effect": the ejection of warm ionized gas from cold molecular clouds. The gas cells inside the Strömgren radii of the H II regions are fully ionized and heated to a temperature of 7000 K.

The dense molecular gas clouds in which star formation occurs are dispersed on short timescales by the momentum from these H II regions, as discussed at length in S. M. R. Jeffreson et al. (2021) and S. M. R. Jeffreson et al. (2024). However, H II region momentum does not contribute substantially to the total momentum injected by stellar feedback across each simulation: in our prescription, the H II region momentum injection is less than 10% of the supernova momentum injection for a given stellar cluster.

3. Star Formation and Interstellar Medium Morphology

Quiescent, bulge-dominated galaxies have been found to have cold gas depletion times that are, on average, substantially longer than those measured for the main-sequence galaxy population (e.g., A. Saintonge et al. 2012; T. A. Davis et al. 2014; D. Colombo et al. 2020). Such elliptical galaxies are also found to have smoother, less fragmented ISMs than their main-sequence counterparts (T. A. Davis et al. 2022; J. Gensior et al. 2023). Figures 4–6 examine the star-forming and gas-morphological properties of our simulated galaxies.

We note that the analysis presented in Figures 3 and 6–13 excludes the central 50 pc of each galactic disk. We excise this region of each simulation for two reasons. First, the scale heights of our simulated ETG gas disks become too small to be sufficiently well resolved in the central 50 pc. Second, we do not account for AGN feedback, which may affect the formation and properties of galactic centers in real galaxies. The excision does not apply to Figures 1 and 2 because these figures compare the global properties of each disk to observations.

3.1. Star Formation

Figure 4 shows the SFR surface density $\Sigma_{\rm SFR}$ of our six simulated galaxies as a function of their cold gas surface densities $\Sigma_{\rm HI+H_2}$, their molecular gas surface densities $\Sigma_{\rm H_2}$, and their stellar surface densities Σ_*. Large circles represent averages over simulation time across the extent of each gas disk. Error bars represent the corresponding interquartile ranges, where the interquartile ranges for the ETGs are too small to be displayed.

The SFR surface densities in Figure 4 are calculated as averages over the preceding 5 Myr, similar to the time interval traced in observations via Hα emission. Observed values from the ATLAS$^{\rm 3D}$ survey (small transparent and open circles) are shown for comparison with the ETG simulations (large filled circles), and the observed position of NGC 300 in the left and middle panels (black transparent star; J. M. D. Kruijssen et al. 2019) is shown for comparison with the late-type simulations (black and turquoise large open circles). The close agreement between simulations and observations in this Figure and in Figure 1 is an important validity check for our numerical models of star formation and stellar feedback, outlined in Section 2.

Five out of six galaxies fall along the typical power law of index $\sim$1.5 (black solid line, left panel) relating the SFR surface density to the cold gas surface density for main-sequence galaxies (R. C. Kennicutt 1998; F. Bigiel et al. 2008). These five galaxies have molecular gas depletion times of 1 Gyr (dashed line, middle panel). However, the ETG with the highest κ displays a suppressed SFR, falling substantially below the power law, with a molecular gas depletion time of around 8 Gyr. That is, star formation in the ETG simulation of stellar mass $M_* = 10^{11}\,M_\odot$ (with the most concentrated stellar bulge) is dynamically suppressed by nearly an order of magnitude in depletion time. We analyze this galaxy in detail in the second paper of this series.

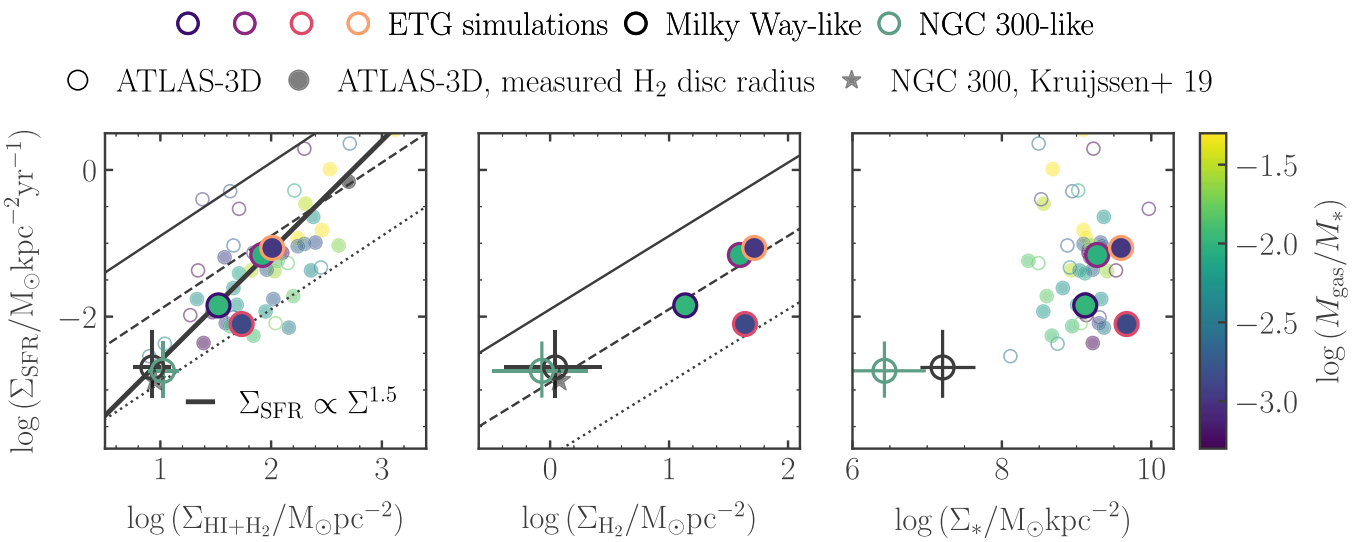

Figure 4. Left: median SFR surface density $\Sigma_{\rm SFR}$ as a function of the cold gas (atomic plus molecular) surface density $\Sigma_{\rm HI+H_2}$, integrated across each simulated galaxy (large circles) and measured for the galaxies in the ATLAS$^{\rm 3D}$ galaxy sample (T. A. Davis et al. 2013, 2014; small transparent circles). The colors of the data points correspond to their gas fractions, and gas depletion times of 10^8, 10^9, and 10^{10} yr are given by the black solid, dashed, and dotted lines, respectively. Interquartile ranges over time and galactocentric radius are given by error bars. For the ETG simulations, these are too small to be shown. Middle: similar to the left panel, but for the molecular gas surface density $\Sigma_{\rm H_2}$. Right: similar to the left panel, but for the median stellar surface density Σ_* across the gas disk.

3.2. Disk Morphology and Fragmentation

The middle and bottom rows of panels in Figure 5 compare the total gas disk surface density $\Sigma_{\rm gas}$ and the molecular gas disk surface density $\Sigma_{\rm H_2}$ of all six galaxy simulations, within 2 kpc patches at face-on and edge-on viewing angles. For the ETG simulations (left four columns), these patches cover the extent of the entire gas disk. For the Milky Way–like and NGC 300–like galaxies (right two columns), with respective gas disk diameters (by eye) of ∼30 and ∼12 kpc, the patch shows only a small portion of each gas disk. The excluded central 50 pc of each gas disk, noted in Section 3.1, is marked by a white circle and is removed from our analysis for the remainder of the paper.

The top row of panels shows the edge-on stellar surface density Σ_* for each galaxy, highlighting the fact that the stellar distribution for the ETGs is bulge dominated ($M_{\rm disk}/M_{\rm bulge} \sim 0.2$), whereas the stellar distribution is disk dominated for the Milky Way–like galaxy ($M_{\rm disk}/M_{\rm bulge} \sim 0.9$) and for the NGC 300–like galaxy ($M_{\rm bulge} \sim 0$).

All four ETG simulations have much smoother gas distributions than do the main-sequence galaxy simulations. While the Milky Way–like and NGC 300–like galaxies display giant feedback-driven voids of several kiloparsecs in diameter, such bubbles are reduced to diameters of <100 pc in the ETGs. The dynamically suppressed ETG ($M_* = 10^{11}\,M_\odot$) is particularly smooth, as expected according to its long cold gas depletion time and thus infrequent stellar feedback. The three other ETGs are manifestly fragmented into dense gas clouds but still remain much smoother than their main-sequence counterparts.

This lower degree of gas disk fragmentation in the ETG simulations, relative to the large spiral (Milky Way–like) simulation, is in qualitative agreement with the observed sample of early-type and spiral galaxies in T. A. Davis et al. (2022). In that work, the disk clumpiness of a sample of 86 spiral galaxies, as quantified by the Gini statistic, is more than double that of a sample of 15 early-type, bulge-dominated galaxies, which vary from very smooth (resembling our dynamically suppressed ETG simulation) to manifestly fragmented (resembling our other ETG simulations). The disk smoothness is also seen to increase with the central stellar surface density in these observations, in qualitative agreement with our $10^{11}\,M_\odot$ ETG, which has the most concentrated stellar bulge and the smoothest gas disk. We will discuss the physical drivers of this disk smoothness in Section 4.

Finally, we note that the gas and stellar disks of our ETG simulations develop a slight kinematic misalignment during their 400 Myr of evolution. This misalignment likely arises as a result of the gravitational interaction between the gas disk and the stellar bulge. The maximum skew of 3° occurs for the smoothest disk with the most compact bulge ($M_* = 10^{11}\,M_\odot$). Throughout this work, the term "midplane" therefore refers specifically to the midplane of the gas disk.

3.3. Gas Phases

The phase structure of the gas in each of our simulations is presented in Figure 6. The top two panels compare the mass-weighted distributions of gas as a function of volume density $n_{\rm H}$ and temperature T ("phase diagrams") for the Milky Way–like and the dynamically suppressed ETG simulation. The phase diagram for the NGC 300–like simulation is very similar to that of the Milky Way, and the phase diagrams of the other three ETGs are relatively similar to that of the quenched ETG. The gas cells are clustered around the state of thermal equilibrium balancing the cooling rate (dominated in our simulations by line emission from C^+, O, and Si^+) and the heating rate due to the photoelectric effect at the surfaces of PAHs and dust grains. The region of the histogram at $T \sim 7000$ K and high volume density corresponds to the gas that is heated by the thermal feedback from H II regions, and the gas above a temperature of ∼20,000 K is heated by supernova feedback.

The bottom left panel of Figure 6 shows the partitioning of the ISM into the four phases that are delineated by dashed lines in the phase diagrams: feedback heated (SN and H II), the warm neutral medium (WNM), the cold neutral medium (CNM), and

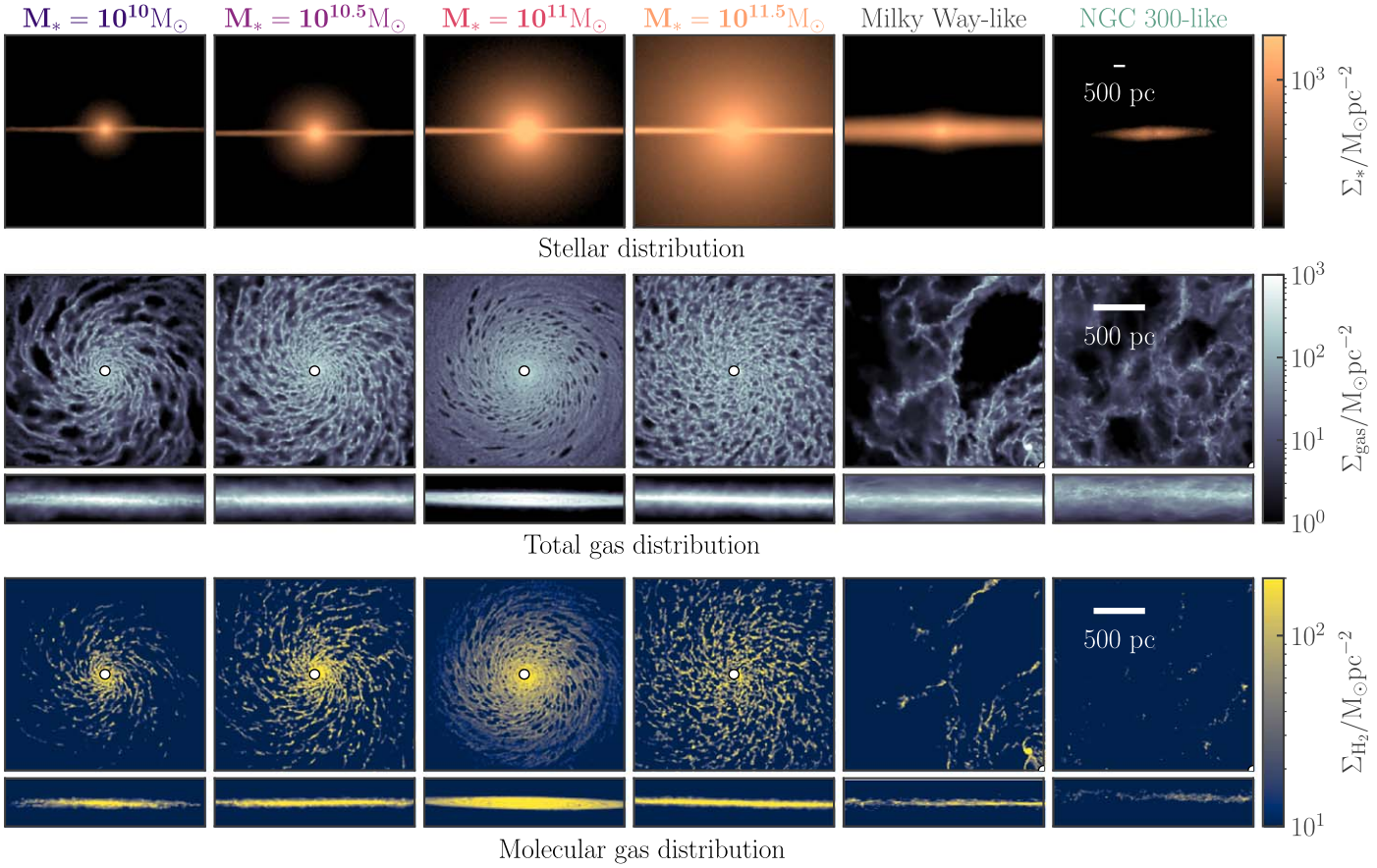

Figure 5. Surface density maps of the stellar distribution viewed parallel to the galactic midplane (Σ_*; top panels), the total gas distribution viewed perpendicular to and parallel to the galactic midplane (Σ_{gas}; middle panels), and the molecular gas distribution viewed perpendicular to and parallel to the galactic midplane (Σ_{H_2}; bottom panels) for each of the simulated galaxies. All ETGs are shown at a simulation time of 400 Myr, while the Milky Way–like galaxy is shown at a simulation time of 600 Myr and the NGC 300–like galaxy is shown at a simulation time of 800 Myr. The small white circles denote the minimum galactocentric radius analyzed in this work. Note that only a small off-center section of the larger Milky Way–like and NGC 300–like disks is displayed.

the molecular hydrogen fraction (H_2). This partitioning is chosen by eye, with the exception of the H_2 mass, which is calculated during the simulation run time using the chemical network described in Section 2. Any H_2 mass contained in the other partitions is subtracted to produce the bar plot.

We see that the star-forming main-sequence (Milky Way–like and NGC 300–like) simulations contain a much higher fraction of hot gas (salmon-colored bars, bottom left) than is present in the ETG simulations, commensurate with their much larger feedback-driven bubbles and voids, as shown in Figure 5. Conversely, the ETG simulations contain a much higher fraction of cold atomic and molecular gas (black and turquoise bars, left panel): up to 70% in the dynamically suppressed ETG, and 40% in the other ETGs, relative to <10% of the gas in the main-sequence galaxies. The much larger fraction of SN-heated gas in the Milky Way–like and NGC 300–like simulations, despite their similar depletion times to three of the ETGs, points to a larger degree of supernova clustering, relative to the ETGs (see, e.g., S. M. R. Jeffreson et al. 2021; M. C. Smith et al. 2021). We will return to this point in Section 4.

The bottom right panel of Figure 6 shows the partitioning of the star-forming gas (gas with $n_H > 100\,cm^{-3}$) into four logarithmic bins of SFE per freefall time ϵ_{ff}, which is computed during the run time of the simulation according to Equation (3). Darker colors correspond to higher values of ϵ_{ff}. The fraction of dense gas that is forming stars, particularly at high ϵ_{ff}, is manifestly larger in the star-forming main-sequence galaxies than in the four ETGs. In particular, the dynamically suppressed ETG displays a much smaller fraction of highly star-forming gas, with $\epsilon_{ff} > 0.5\%$ (less than half of the fraction in the other three ETGs). Despite having a much higher molecular fraction than the other ETGs, it contains no gas with $\epsilon_{ff} > 5\%$. The dynamical suppression of star formation in one out of four ETG simulations therefore occurs as a result of the reduction of ϵ_{ff} in the coldest and densest molecular gas.

4. Supernova Clustering, Galactic Outflows, and the Equation of State

Recent numerical work has shown that supernova clustering is likely to enhance the strength and mass loading of galactic outflows (C.-G. Kim et al. 2017; D. Fielding et al. 2018; S. M. R. Jeffreson et al. 2021; M. C. Smith et al. 2021), perhaps at the expense of turbulence driving within the ISM (M. E. Orr et al. 2022). In turn, the majority of supernova clustering occurs in the most massive GMCs (S. M. R. Jeffreson et al. 2024), which host the majority of galactic star formation (N. Murray & M. Rahman 2010). These massive clouds are able to grow owing to a high rate of accretion from the galactic environment, and they display substantially higher lifetime SFEs than their low-mass counterparts, as they are slightly more difficult to destroy (e.g., N. Murray et al. 2010; M. Y. Grudić et al. 2018; S. M. R. Jeffreson et al. 2024).

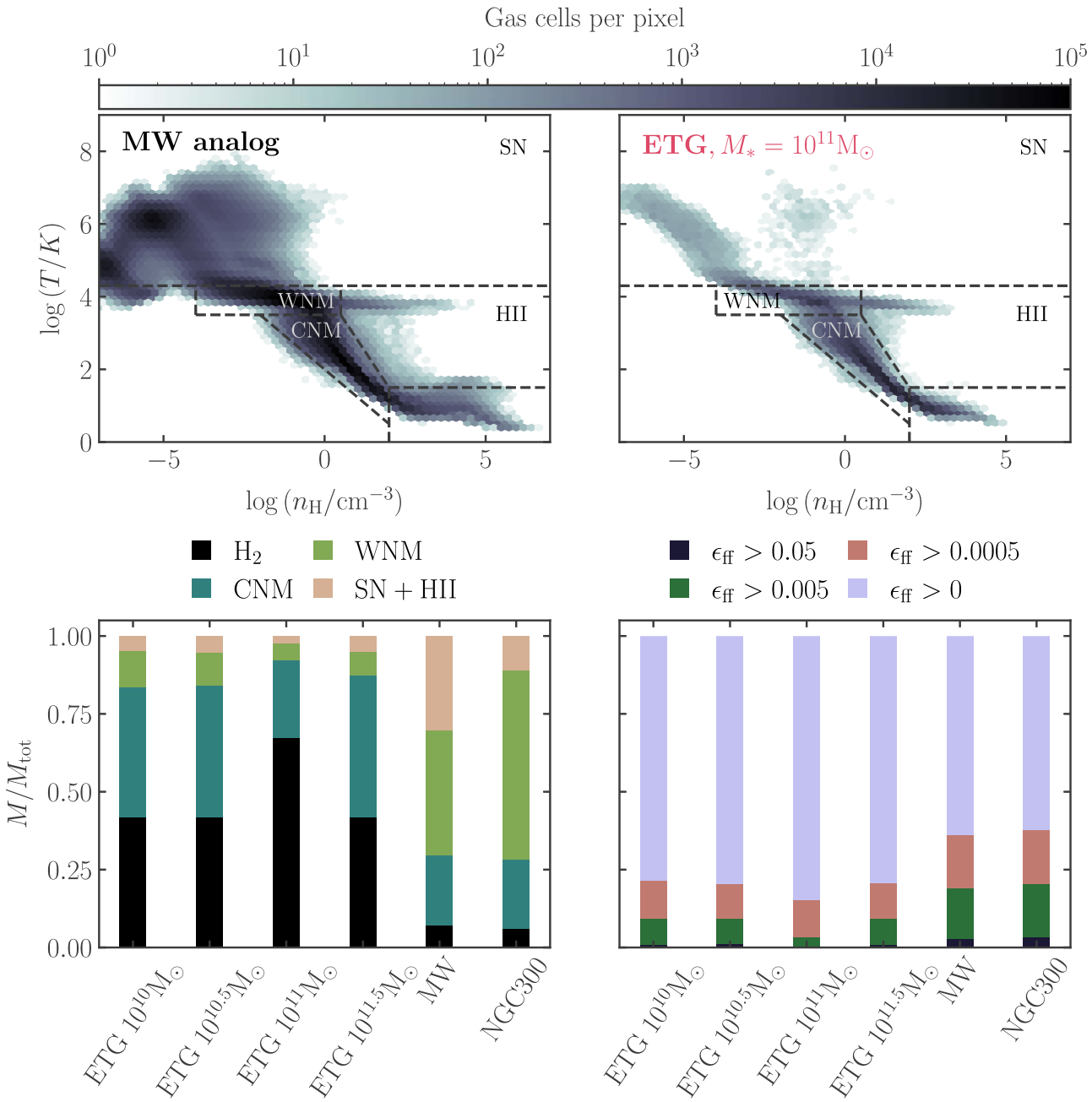

Figure 6. Top panels: density–temperature phase diagrams for the Milky Way–like galaxy simulation (left) and the smoothest ETG ($M_* = 10^{11}\ M_\odot$; right). Dashed lines delineate the regions of phase space corresponding to the bar plot in the bottom panels. Bottom left: partitioning of the gas mass in each simulation into four ISM phases, from warmest to coolest, as a fraction of the total gas mass in the simulation: hot gas that has received thermal energy from stellar feedback ($M_{\mathrm{SN+HII}}$), the WNM (M_{WNM}), the CNM (M_{CNM}), and the total molecular hydrogen reservoir ($M_{\mathrm{H_2}}$). The molecular hydrogen mass is subtracted from each of the other phase-space regions to produce the bar plot. Bottom right: partitioning of the star-forming gas mass with density $\rho/m_{\mathrm{H}}\mu > 100\ \mathrm{cm}^{-3}$ into fractions with differing SFEs per freefall time, ϵ_{ff}.

In the following sections, we discuss the connection between the rotational support of the gas disk, supernova clustering, and galactic outflow strength across our main-sequence and quenched galaxy simulations. We then demonstrate the impact of this physics on the EOS (pressure vs. density relation) and its implications for modeling gas in cosmological simulations.

4.1. Disk Stability and Toomre Length

The top row of panels in Figure 7 demonstrates that the ETGs in our galaxy sample have a much greater level of disk stability than the main-sequence galaxies. We calculate the Toomre Q parameter for a multiphase ISM of finite disk thickness (as is appropriate to our simulations) via the prescriptions of A. B. Romeo & J. Wiegert (2011) and A. B. Romeo & N. Falstad (2013), which are in close agreement.[15] A. B. Romeo & J. Wiegert (2011) combine separate gas and stellar contributions to the dispersion relation, while A. B. Romeo & N. Falstad (2013) additionally consider separate contributions from the molecular, atomic, and ionized

[15] The hot phase ($T > 2 \times 10^4$ K) is excluded, as the majority of this gas is contained in feedback-driven bubbles or galactic outflows and so does not contribute to the disk.

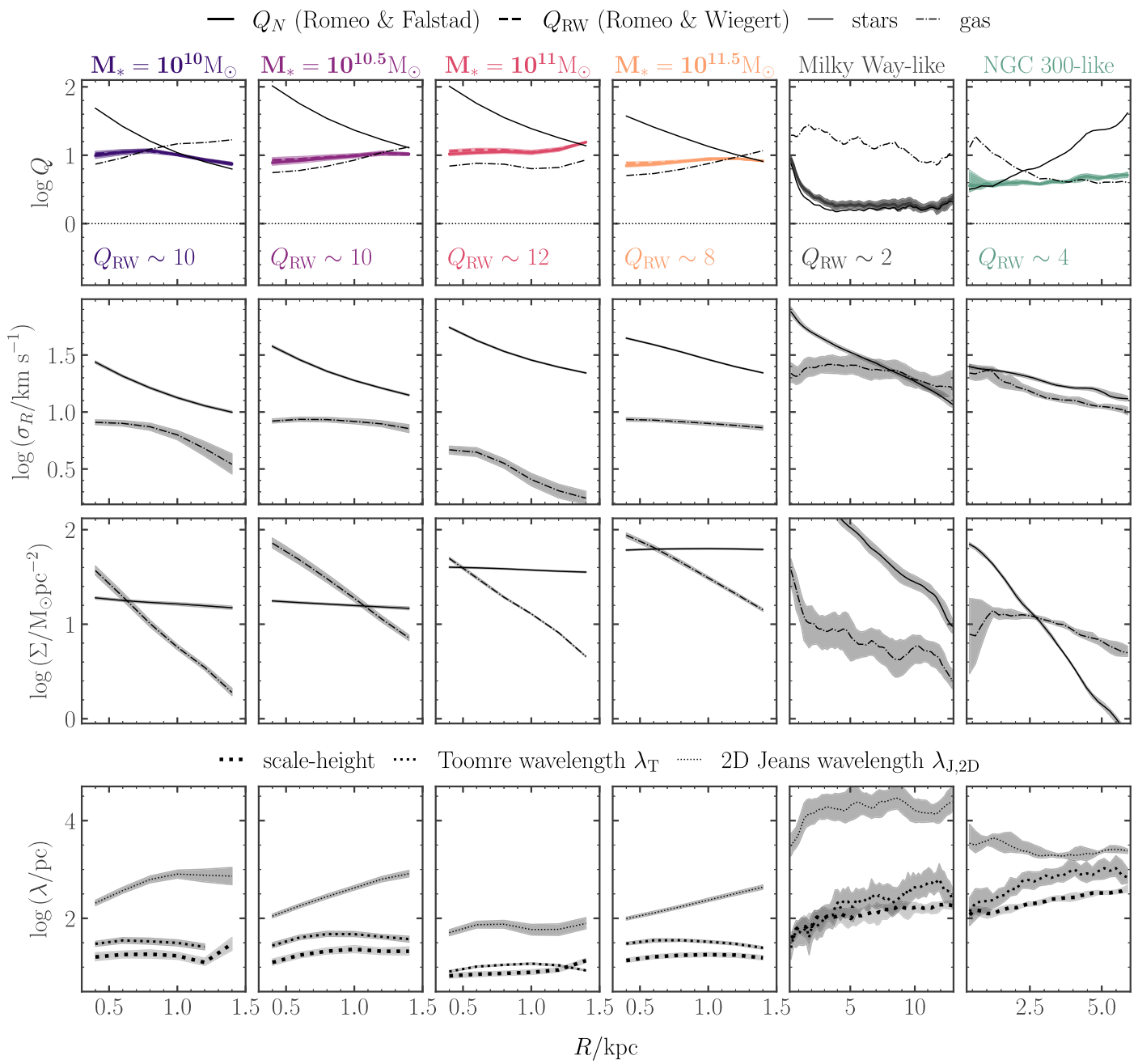

Figure 7. The median Toomre Q parameter (top row), gas and stellar radial velocity dispersion (second row), and gas and stellar surface density (third row) as a function of galactocentric radius for the six galaxies in our sample. The bottom row compares the gas disk scale height to the Toomre and 2D Jeans wavelengths. All values are computed for gas at temperatures $T < 2 \times 10^4$ K. Shaded regions represent interquartile ranges over azimuthal angle and simulation time. The Toomre Q parameters of the ETGs are much higher than those of the main sequence (Milky Way–like and NGC 300–like) galaxies.

gas phases. The solid and dotted–dashed lines show the stellar and gaseous Toomre Q parameters $Q_* = \kappa\sigma_{R,*}/3.36G\Sigma_*$ and $Q_{\rm gas} = \kappa\sigma_{R,{\rm gas}}/\pi G\Sigma_{\rm gas}$, respectively, where κ is the epicyclic frequency $\kappa^2 = R^{-3}d(\Omega^2R^4)/dR$ (shown in Figure 3), $\sigma_{R,*}$ and $\sigma_{R,{\rm gas}}$ (see Appendix B) are the radial stellar and gas velocity dispersions (shown in the second row of panels), and Σ_* and $\Sigma_{\rm gas}$ are the stellar and gas surface densities (shown in the third row of panels).

Comparing Figures 7 and 3, we see that the elevated disk stability in the ETGs is driven primarily by the stellar contribution to galactic rotation. Though the gas and stellar velocity dispersions in the ETGs are actually lower than those in the outer Milky Way and the gas and stellar surface densities are comparable, compact stellar bulges in the four ETGs drive up their epicyclic frequencies κ by around an order of magnitude. This translates to a substantial increase in their Toomre Q values.

We caution that the Toomre Q parameters in Figure 7 are shown only as a comparison of the approximate level of stability between the six simulations. In turbulent media, the classical threshold, predicting fragmentation only for $Q \leqslant 1$, does not strictly apply. First, the threshold for axisymmetric disk instability is a more complicated function of a and b, where the gas surface density has a length scaling relation of $\Sigma \propto \ell^a$ and the velocity dispersion has a scaling relation of $\sigma \propto \ell^b$ (e.g., A. B. Romeo et al. 2010). There exist non-Toomre regimes of a and b in which small or large scales may always

be unstable (e.g., A. B. Romeo et al. 2010; P. F. Hopkins & J. L. Christiansen 2013). Furthermore, the original Toomre Q criterion does not take account of nonaxisymmetry or vertical dynamics, magnetic effects, nonlinearity (e.g., W.-T. Kim & E. C. Ostriker 2001; W.-T. Kim et al. 2002), or turbulent dissipation (e.g., B. G. Elmegreen 2011). The fact that $Q \approx 10$ for our ETGs does not imply that gravitational fragmentation is not occurring in these galaxies, and drawing a quantitative conclusion from Q alone is discouraged.

The bottom row of Figure 7 compares the cold+warm gas disk scale height (thick dotted lines) for each simulation to its Toomre wavelength $\lambda_{\rm T} = (2\pi)^2 G \Sigma_{\rm gas}/\kappa^2$ (intermediate dotted lines) and its 2D Jeans wavelength (thin dotted lines). Due to its higher rate of galactic rotation, the Toomre wavelength associated with the dynamically suppressed ETG simulation (stellar mass $M_* = 10^{11}\,M_\odot$; pink label) is about one-third the value of the other three ETGs.

Comparing Figures 7 and 5, we see that smoother gas morphologies and smaller voids in the gas distribution are associated with the shorter Toomre wavelengths $\lambda_{\rm T}$ of the ETGs. That is, angular momentum imposes much stronger constraints on the scale of self-gravitating condensation for the ETGs. Because the variation in the ratio σ_R/Σ is much smaller than that of $\lambda_{\rm T}$, this also means that smoother gas distributions are associated with higher Toomre Q values, as observed by T. A. Davis et al. (2022). In the next subsection, we will show that this smoother gas distribution is associated with a lower level of supernova clustering and weaker galactic outflows.

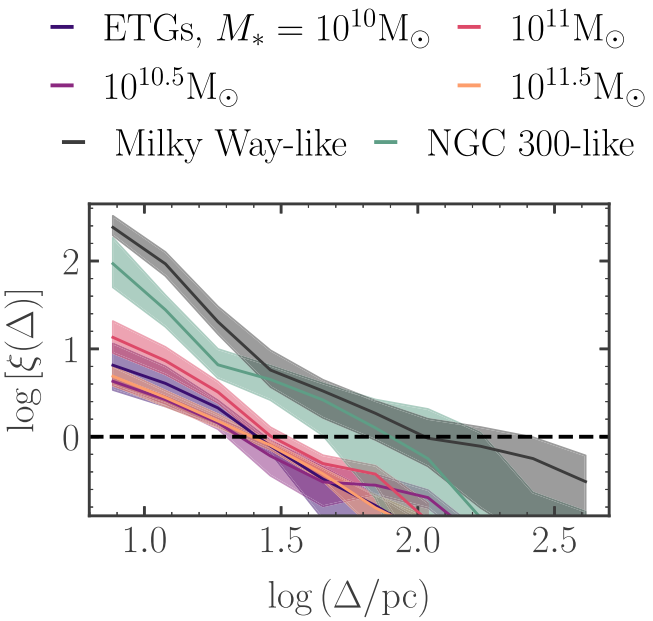

Figure 8. The two-point correlation function $\xi(\Delta)$ for supernova explosions (quantifying the degree of supernova clustering) as a function of their separation Δ over time intervals of 1 Myr, averaged over all times throughout each simulation (solid lines). The black dashed line indicates the profile for a uniform distribution of objects across the galactic midplane ($\xi(\Delta) = 1$). The shaded regions give the interquartile ranges over these times. The level of supernova clustering is higher on all scales in the Milky Way–like and NGC 300–like simulations, relative to the ETG simulations.

4.2. Supernova Clustering

Figure 8 shows the level of supernova clustering in each of our simulated galaxies, quantified by the two-point correlation function $\xi(\Delta)$ of supernova explosions as a function of spatial scale Δ. If $\xi > 1$, then the supernovae are more clustered than would be expected for a uniform distribution of objects across the galactic midplane; if $\xi < 1$, then they are less clustered. The supernovae in the star-forming main-sequence galaxy simulations display much stronger clustering on all scales than do the ETG simulations (up to an order of magnitude in ξ). The Milky Way–like and NGC 300–like simulations display substantial supernova clustering at all scales below $\Delta \sim 100$ pc, while the ETG simulations display supernova clustering only on much smaller scales, below $\Delta \sim 25$ pc.

The level of supernova clustering is clearly associated with the length scale of gravitational instability $\lambda_{\rm T}$ in each disk (Figure 7), and thus with the epicyclic frequency κ, dependent on the rotational shear $d\Omega/d\ln R$ (Figure 3). In particular, the onset of clustering, indicated by the intercept of the black dashed line in Figure 8, occurs at approximately the Toomre length for each simulated disk. As seen in the bottom row of Figure 7, this Toomre length scale is substantially smaller in the ETG models, and this stricter limit from angular momentum on the outer scale of self-gravitating condensation is reflected in the lower level of SN clustering seen in Figure 8. A similar trend of increasing outflow strength with increasing instability scale (due to increasing box size) is also noted in Appendix A of C.-G. Kim et al. (2020). In other words, these galactic dynamics influence the clumpiness of the ISM (the freefall times of the most massive GMCs; see Figure 14 of S. M. R. Jeffreson et al. 2024) and therefore the clumpiness of supernova explosions.

4.3. Galactic Outflows

Figure 9 shows the total galactic SFR (top panel), the rate of gas outflow ($\dot{M}_{\rm out}$; middle panel), and the mass loading η of the galactic outflows (bottom panel) in each of our simulated galaxies, as a function of simulation time. We begin tracking each property only after each disk has reached a state of dynamical equilibrium. The outflow rates are calculated as the total momentum (volume) density of the gas moving away from the disk, integrated over the area of two planar slabs of thickness 500 pc, located at ± 1 kpc above and below the galactic disk, i.e., the mass flux $\dot{M}_{\rm out} = \int dA\ \rho v_z$. The mass loading divides this outflow rate by the SFR.

The strength and mass loading of the outflows display a very large difference of around 3–4 orders of magnitude between the star-forming main-sequence galaxy simulations and the ETG simulations. This difference could be attributed to two factors: (1) the increased levels of supernova clustering in the Milky Way–like and NGC 300–like simulations (Figure 8), and (2) the shallower gravitational potential wells of these galaxies. A shallower gravitational potential well, measured perpendicular to the galactic midplane, decreases the escape speed perpendicular to the midplane.

The role of supernova clustering alone in driving strong galactic outflows can be quantified by comparing the Milky Way–like galaxy and the ETG of stellar mass $M_* = 10^{10.5}\,M_\odot$, which have similar average values of the gravitational potential (and thus escape speed) across the extents of their respective gas disks, at the distance of 1 kpc from the galactic midplane at which the outflow is measured. Figure 9 demonstrates that these two galaxies nevertheless have very different values of the outflow rate and mass loading, which are therefore attributable solely to their very different levels of supernova clustering,

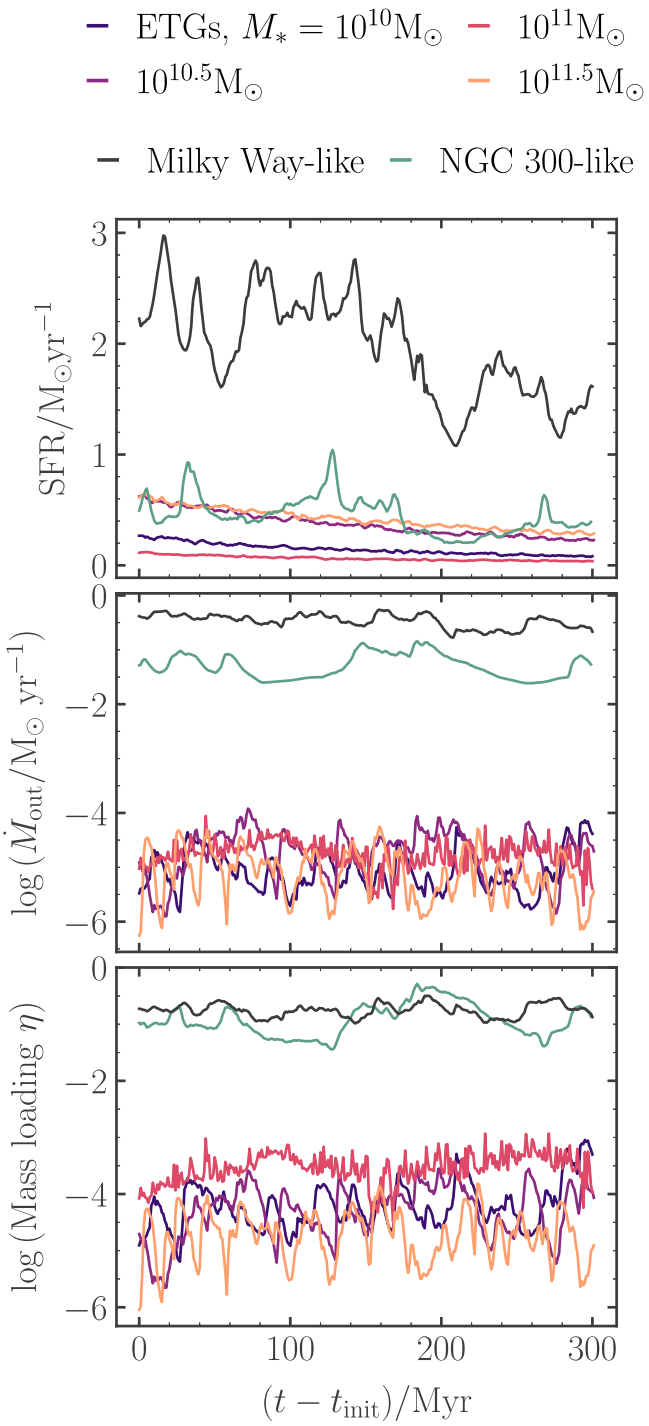

Figure 9. Global galactic SFR (top panel), gas outflow rate (middle panel), and mass loading of outflows (bottom panel) as a function of time. We begin tracking each property only when the gas disks have reached a state of dynamical equilibrium: 100 Myr onward for the ETG simulations, 300 Myr onward for the Milky Way–like simulation, and 500 Myr onward for the NGC 300–like simulation.

mediated by the level of galactic rotation and the associated level of disk gravitational stability Q and the Toomre wavelength.

4.4. The Effective Equation of State of the Cold+Warm Gas Distribution

The turbulent and thermodynamic state of the cold+warm gas reservoir ($T < 2 \times 10^4$ K) in each galaxy can be described by an EOS relating the total turbulent plus thermal gas midplane pressure P_{tot} to the midplane gas density $n_H = \rho/(\mu m_p)$, where μ is the mean molecular weight. This EOS is equivalent to a statement of the combined turbulent and thermal gas velocity dispersions, as $P_{tot} \equiv P_{th} + P_{z,turb} \sim \rho(c_s^2 + \sigma_{z,turb}^2)$, where c_s is the isothermal sound speed. The EOS therefore depends on the momentum and energy injected by stellar feedback, which is a key driver of turbulence.

Because this cold+warm reservoir of star-forming gas is unresolved in cosmological simulations, it is necessary to parameterize the EOS in terms of its properties on large, resolved scales. This fixed, "effective" EOS (eEOS) therefore provides an effective pressure that accounts for the unresolved stellar feedback in the simulation.

In Figure 10, we demonstrate how such an eEOS can be derived from our high-resolution GalactISM simulations, with star-forming gas reservoirs resolved on scales of 1–100 pc in the warm+cold gas reservoir. Filled data points represent median values of the total midplane pressure P_{tot} and density n_H, as well as the epicyclic frequency κ, within overlapping radial annuli of width 500 pc. Our method for calculating P_{th}, P_{turb}, and ρ is outlined in Appendix B.

In the left panel of Figure 10, we show the standard two-dimensional eEOS, characterized by the variables n_H and P_{tot}. The best fit to our two star-forming main-sequence galaxies (the Milky Way–like and NGC 300–like simulations in gray and green, respectively) is given by a thick black line and takes the form

$$\log(P_{tot}/k_B) = 1.14 \log(n_H/\mathrm{cm}^{-3}) + 4.42. \quad (4)$$

This can be compared to the best-fit eEOS in star-forming main-sequence environments reported in E. C. Ostriker & C.-G. Kim (2022) from TIGRESS simulations, given by $\log(P_{tot}/k_B) = 1.43 \log(n_H/\mathrm{cm}^{-3}) + 4.30$ and denoted by the black dashed line. The two fits are in relatively good agreement, albeit with Equation (4) having a slightly shallower slope than the TIGRESS fit. This difference reflects detailed differences between the feedback models and is not unexpected. In fact, with the updated TIGRESS-NCR framework, a shallower slope is obtained than with the original TIGRESS framework (C.-G. Kim et al. 2023a).

In the middle and right panels of Figure 10, we show that the ETG simulations in our sample have different EOSs from the Milky Way–like and NGC 300–like simulations, overlapping only with the centermost regions of the main-sequence galaxies. As the level of galactic rotation is increased, the eEOS is shifted systematically toward lower gas velocity dispersions. That is, the support against gravitational collapse that is provided by galactic rotation allows gas to remain gravitationally stable at higher densities and lower velocity dispersions, commensurate with the smaller Toomre wavelengths λ_T, smaller scale heights, and lower levels of supernova clustering, as reported in Figures 7 and 8.

Our simulations provide evidence that rotationally supported regions in galaxies (including the central regions of the Milky Way–like galaxy) have reduced thermal and turbulent pressure and potentially require an adjusted eEOS in cosmological simulations. The gray transparent plane in Figure 10 shows such a three-dimensional eEOS, characterized by the variables n_H, P_{tot}, and κ and fitted to all galaxies in the simulation suite, excluding the ETG with dynamically suppressed star formation

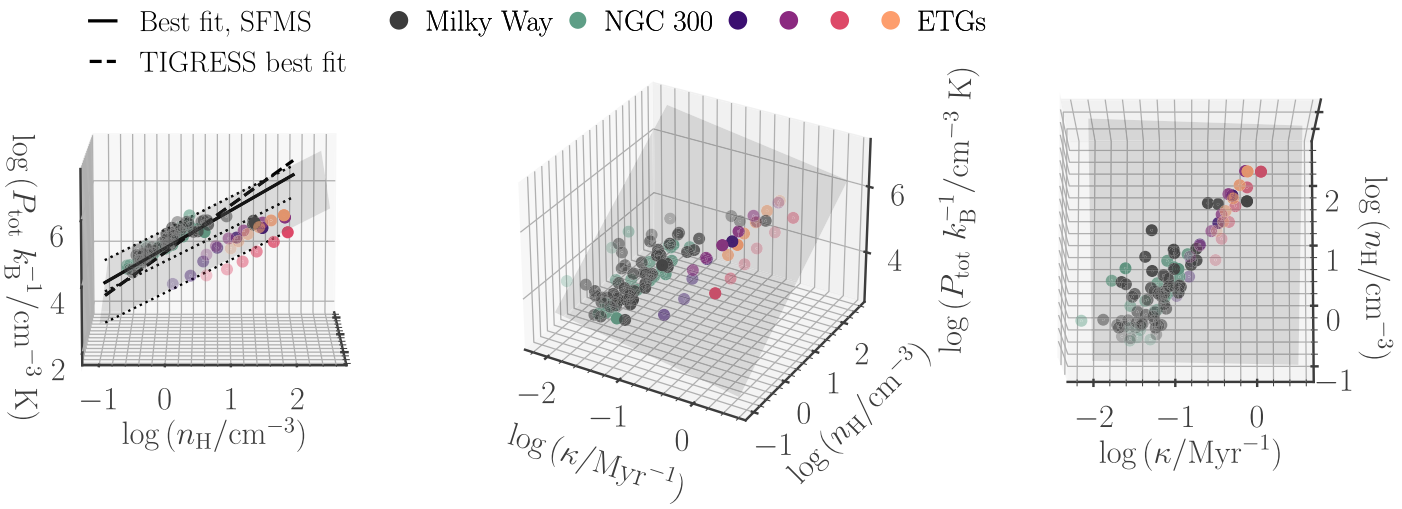

Figure 10. Total midplane pressure $P_{\rm tot}$ as a function of the midplane gas volume density $n_{\rm H}$ and the epicyclic frequency κ for the cold+warm gas ($T < 2 \times 10^4$ K) in our simulations, viewed in three different planes. The left panel shows the usual EOS ($P_{\rm tot}$ vs. $n_{\rm H}$) for our simulated galaxies. The best-fit line to the Milky Way and NGC 300 (star-forming main-sequence) galaxy simulations is given by the solid black line, and the best fit to the TIGRESS simulations is indicated by the thick dashed line. Three isotherms of constant $T = P_{\rm tot}/n_{\rm H}k_{\rm B}$ are given by gray dotted lines. Filled data points represent median values over time and azimuthal angle for each simulated galaxy, measured within overlapping radial annuli of width 500 pc. The gray transparent plane shows the best fit to all data, excluding the dynamically suppressed galaxy (pink).

(pink data points). This best fit takes the form

$$\log(P_{\rm tot}/k_{\rm B}) = -0.33\log(\kappa/{\rm Myr}^{-1}) + 1.03\log(n_{\rm H}/{\rm cm}^{-3}) + 3.93. \quad (5)$$

If κ displays only a small variation between galaxies, then we obtain $\log P_{\rm tot} \propto 1.03 \log n_{\rm H}$, which is close to the best-fit two-dimensional eEOS reported in Equation (4).

Finally, we note that the dynamically suppressed ETG is offset from the plane characterizing the star-forming gas in the other five galaxies. In a future paper, we will investigate in detail how this behavior is related to the rate of galactic rotation, leading to a transition to a longer depletion time, lower gas velocity dispersion, and smaller gas disk scale height, which is nonlinear in κ.

5. Star Formation Regulation

Power-law relationships between the SFR surface density $\Sigma_{\rm SFR}$ and other large-scale properties of galaxies provide important constraints for theories of galactic star formation. They also function as subgrid models for star formation in cosmological simulations, in which the cold+warm ISM cannot be resolved. Most commonly, such subgrid models are underpinned by the empirical power-law relationship between $\Sigma_{\rm SFR}$ and either the neutral gas surface density $\Sigma_{\rm HI+H_2}$ or the molecular gas surface density $\Sigma_{\rm H_2}$. Crucially, their slopes and normalizations are calibrated to observed samples of galaxies, limiting their predictive power and applicability to a diverse set of galactic environments. In this section we test a new, predictive subgrid model for star formation in disk galaxies.

5.1. Gas Surface Density versus Star Formation Rate Surface Density

The most common subgrid model for star formation in cosmological simulations sets a depletion time of $\tau_{\rm dep} = m_{\rm cell}/{\rm SFR}_{\rm cell} = \tau_{\rm dep,\,0}(\rho_{\rm thresh}/\rho_{\rm gas})^{0.5}$ per star-forming gas cell of mass $m_{\rm cell}$, where $\rho_{\rm gas}$ is the volume density of the gas, $\rho_{\rm thresh}$ is the density above which star formation is allowed to occur, and $\tau_{\rm dep,\,0}$ is the gas depletion time at this threshold. The resulting inverse proportionality between the SFR and the gas freefall time $\sqrt{3\pi/32G\rho_{\rm gas}}$ is in rough agreement with a sample of 21 observed spiral galaxies at low redshift from R. C. Kennicutt (1998), which follow the power law $\Sigma_{\rm SFR} \propto \Sigma_{\rm HI+H_2}^{1.4}$, averaged across galactic disks (the "Schmidt–Kennicutt relation"). This model is used in IllustrisTNG (V. Springel & L. Hernquist 2003; M. Vogelsberger et al. 2013) and is qualitatively very similar to the models used in other large cosmological simulations, such as EAGLE (J. Schaye et al. 2015).[16]

The solid black line and shaded region in the left panel of Figure 11 represent the median and interquartile range of this subgrid model, when applied to the outputs of our GalactISM simulations, degraded to the TNG-50 resolution of 80 pc. For comparison, the filled data points represent the true median values of $\Sigma_{\rm HI+H_2}$ and $\Sigma_{\rm SFR}$ in each simulation, within overlapping radial annuli of width 500 pc. The blue contours in the left panel represent the sample of 18 galaxies observed at 750 pc by F. Bigiel et al. (2008), and the gray contours in the right panel represent the sample of 80 galaxies observed at 1.5 kpc resolution by J. Sun et al. (2023).

We note that the slight ($\approx$0.3 dex) overestimate of the SFR surface density $\Sigma_{\rm SFR}$ for our Milky Way–like simulation, relative to the 95% confidence level of the F. Bigiel et al. (2008) values, is likely due to differences in the stellar gravity for given $\Sigma_{\rm HI+H_2}$. First, the AGORA initial condition has a smaller stellar disk scale height than the Milky Way–like galaxies observed by F. Bigiel et al. (2008), as we mentioned in Section 2.1.2. Second, the fraction of ionized gas is enhanced, as seen in Figure 6, and thus $\Sigma_*/\Sigma_{\rm HI+H_2}$ is slightly increased, relative to these observed galaxies.

[16] We note that the EAGLE simulations set ${\rm SFR}_{\rm cell}/m_{\rm gas}$ according to a power law in the gas pressure, but in combination with their eEOS $P \propto \rho_{\rm gas}^{4/3}$ above $n_{\rm H} = 0.1$ cm^{-3}, the resulting relation is ${\rm SFR}_{\rm cell}/m_{\rm cell} \propto \rho_{\rm gas}^{0.3}$, and the normalization of this relationship is again set according to R. C. Kennicutt (1998).

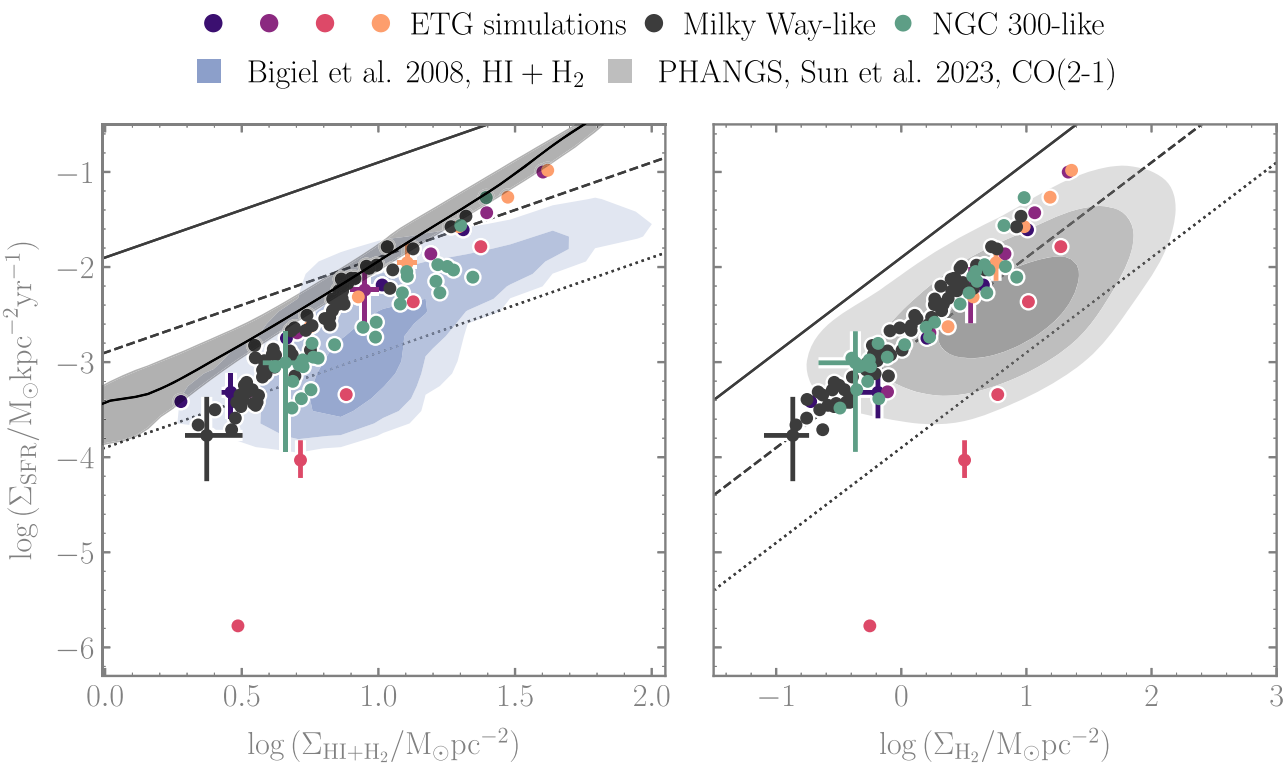

Figure 11. SFR surface density $\Sigma_{\rm SFR}$ as a function of the cold gas surface density $\Sigma_{\rm HI+H_2}$ (left) and as a function of the molecular gas surface density $\Sigma_{\rm H_2}$ (right). Solid, dashed, and dotted lines represent depletion times of 10^8, 10^9, and 10^{10} Gyr, respectively. Filled data points represent median values over time for each simulated galaxy, measured within overlapping radial annuli of width 500 pc. For visual clarity, the corresponding interquartile ranges are shown at just one representative radius in each galaxy. The solid black line and shaded region represent the median and interquartile range of the SFR predicted by the model of V. Springel & L. Hernquist (2003). The model is applied to all of our high-resolution snapshots at once, where each snapshot is degraded to a 3D resolution of 80 pc—equal to the softening length used in TNG-50 (see Section 5.1). The blue and gray contours represent the 40%–80%–95% levels of the observed galaxy samples from F. Bigiel et al. (2008) and J. Sun et al. (2023), respectively, which assume a constant CO-to-H_2 conversion factor.

At a given $\Sigma_{\rm HI+H_2}$, the effect of decreasing the stellar disk scale height and increasing Σ_* is to vertically compress the gas at the galactic midplane, increasing its volume density, pressure, and SFR. In addition, the deviation between simulations and observations at high gas surface densities may be increased by the uncertainty in the CO-to-H_2 conversion factor used in F. Bigiel et al. (2008), since a constant CO-to-H_2 conversion factor tends to overestimate $\Sigma_{\rm H_2}$ in dense galactic centers (see below).

We see that the V. Springel & L. Hernquist (2003) subgrid model provides a reasonable approximation to the median-resolved SFR surface density across the inner regions of the Milky Way–like galaxy simulation (black data points) but overestimates the SFR in the outer regions and fails to capture the variation in depletion time across the NGC 300–like and ETG simulations. Similarly, it does not capture the spread of resolved depletion times in the F. Bigiel et al. (2008) observations. This is perhaps unsurprising, considering that the slope and normalization of the power-law subgrid model are calibrated to galaxy-averaged values in nearby spirals, with physical properties closest to those of our Milky Way–like simulation.

An alternative empirical subgrid model for star formation in cosmological simulations sets the depletion time according to the molecular gas volume density, which in turn is computed via the subgrid model of M. R. Krumholz & N. Y. Gnedin (2011). Similarly to the IllustrisTNG model, the slope and normalization of the power law are set according to the R. C. Kennicutt (1998) galaxy sample. This approach is used in the MUFASA (R. Davé et al. 2016) and SIMBA (R. Davé et al. 2019) simulations and takes advantage of the relatively constant slope of the relationship between the molecular gas surface density $\Sigma_{\rm H_2}$ and SFR surface density, shown in the right panel of Figure 11. The trend across five out of six of our simulated galaxies can be well modeled by a linear relationship between $\Sigma_{\rm SFR}$ and $\Sigma_{\rm H_2}$, with a roughly constant molecular gas depletion time of 1 Gyr. Aside from a slight upturn in $\Sigma_{\rm SFR}$ relative to $\Sigma_{\rm H_2}$ at high surface densities, the simulated data are in good agreement with recent observations of the molecular gas distribution across a sample of 80 nearby galaxies at 1.5 kpc resolution (J. Sun et al. 2023, green contours).

However, although $\Sigma_{\rm H_2}$ appears to be a better predictor of $\Sigma_{\rm SFR}$ than $\Sigma_{\rm HI+H_2}$ (see also, e.g., F. Bigiel et al. 2011), the proportionality between these variables is still an empirical relationship that is calibrated to a set of observations. This relationship is not derived from first principles, so it is not predictive in new galactic environments. Furthermore, new observations of CO isotopologues across nearby galaxies are now revealing substantial variations in the CO-to-H_2 conversion factor $\alpha_{\rm CO}$ (used to derive $\Sigma_{\rm H_2}$) between galaxy disks and galaxy centers (J. S. den Brok et al. 2023; Y.-H. Teng et al. 2023). These results strongly imply that the proportionality between $\Sigma_{\rm SFR}$ and $\Sigma_{\rm H_2}$ is not as universal as previously thought, even across the population of nearby galaxies. In fact, if the variation in the CO-to-H_2 conversion factor is taken into account, the upturn in $\Sigma_{\rm SFR}$ relative to $\Sigma_{\rm H_2}$ that is seen in our simulations at high surface densities would be retrieved in observations (Y.-H. Teng et al. 2023). More generally,

observational evidence has demonstrated that the correlation of star formation with chemical composition (such as CO or HCN) is much weaker when environmental variation is taken into account (e.g., M. J. Gallagher et al. 2018).

An alternative approach to using empirical relations for subgrid SFRs is to predict these SFRs via a theoretical model. In the next subsection, we compare our results to the predictions of the pressure-regulated feedback-modulated star formation theory, calibrated to the TIGRESS simulations (E. C. Ostriker & C.-G. Kim 2022).

5.2. Midplane Pressure versus Star Formation Rate Surface Density

Recent analyses of a large sample of main-sequence galaxies from the PHANGS-ALMA sample (A. K. Leroy et al. 2021) have demonstrated a close correlation between the kiloparsec-scale midplane pressure $P_{\rm tot}$ of gas disks in dynamical equilibrium and the galactic SFR surface density $\Sigma_{\rm SFR}$ (J. Sun et al. 2023), as well as the fraction of dense and self-gravitating molecular gas (J. Sun et al. 2020).

Such a relationship between the SFR and the midplane pressure is a central tenet of "pressure-regulated" theories of star formation (E. C. Ostriker et al. 2010; C.-G. Kim et al. 2011; E. C. Ostriker & R. Shetty 2011). In this theoretical framework (see E. C. Ostriker & C.-G. Kim 2022), the thermal, turbulent, and magnetic pressures in the diffuse ISM are driven by stellar feedback, as offset by dissipation and cooling (see also related work by T. A. Thompson et al. 2005; P. F. Hopkins et al. 2011; C.-A. Faucher-Giguère et al. 2013, on the balance between momentum injection by feedback and turbulent dissipation). That is, there is a causal relationship whereby higher SFRs $\Sigma_{\rm SFR}$, associated with higher fractions of dense, gravitationally bound gas, produce more feedback, and this leads to higher total pressures $P_{\rm tot}$. In the Ostriker–Kim theory, the sum of the pressures $P_{\rm tot}$ must also satisfy vertical dynamical equilibrium by balancing the ISM weight at the midplane. As a result, $\Sigma_{\rm SFR}$ is expected to be directly proportional to the diffuse ISM weight and inversely proportional to the total "feedback yield."

The predicted relationship between $P_{\rm tot}$ and $\Sigma_{\rm SFR}$ is reproduced in simulations of stratified boxes representing a range of observable galactic environments (e.g., C.-G. Kim et al. 2013; C.-G. Kim & E. C. Ostriker 2015; E. C. Ostriker & C.-G. Kim 2022). The required condition of vertical dynamical equilibrium is also demonstrated in these simulations, as well as in the Milky Way–like galaxy of S. M. Benincasa et al. (2016) and FIRE cosmological zoom-in simulations analyzed by A. B. Gurvich et al. (2020). The $P_{\rm tot}$–$\Sigma_{\rm SFR}$ relation has not yet been investigated in high-resolution isolated galaxy simulations spanning diverse galactic environments outside of the star-forming main sequence.

The left panel of Figure 12 shows the relationship between $P_{\rm tot}$ and $\Sigma_{\rm SFR}$ within overlapping radial annuli of width $\sim$500 pc, for diffuse gas in our simulated galaxies.[17] Our method for calculating the total (turbulent plus thermal) midplane pressure is described in Appendix B. The best fit to these data (thick black line), excluding the dynamically suppressed galaxy (pink data points), is given by

$$\log_{10}\left(\frac{\Sigma_{\rm SFR}}{M_\odot\ {\rm kpc}^{-2}\ {\rm yr}^{-1}}\right) = 1.235\log\left(\frac{P_{\rm tot}\,k_{\rm B}^{-1}}{{\rm cm}^{-3}\ {\rm K}}\right) - 7.86. \quad (6)$$

This best fit shows good agreement with the observed relationship between $\Sigma_{\rm SFR}$ with $P_{\rm tot}$ across a sample of 80 nearby galaxies at 1.5 kpc scales (J. Sun et al. 2023), in which SFRs are traced by Hα + 22 μm emission and gas is traced by 21 cm + CO (2–1) emission, with a CO (2–1)/(1–0) conversion factor of 0.65 and a constant CO-to-H_2 factor $\alpha_{\rm CO} = 4.35\ M_\odot\ {\rm pc}^{-2}({\rm K\ km\ s}^{-1})^{-1}$.[18] The resulting logarithmic correlation between $P_{\rm tot}$ and $\Sigma_{\rm SFR}$ for the observed galaxies has a slope of 0.93 and a normalizing coefficient of −6.95, with estimated upper-limit uncertainties of around 25% and 0.20 dex, respectively.

The slightly steeper slope in our simulations may be due to a number of effects. One is that the value of the CO-to-H_2 conversion factor $\alpha_{\rm CO}$ is known to decrease in high-pressure (and high surface density) regions of galaxies (e.g., Y.-H. Teng et al. 2023, and references therein) and is thus not well represented by a constant $\alpha_{\rm CO}$. In fact, using the variable $\alpha_{\rm CO}$ of A. D. Bolatto et al. (2013), J. Sun et al. (2023) find that the slope increases to 1.08. Other possible reasons for the small discrepancy in slopes are (1) differences in the gas and star formation reservoirs that we have analyzed, relative to those traced by CO and Hα emission in the observations; (2) a small underestimate of the momentum provided by feedback at high pressures/densities, in our simulated galaxies; and (3) variation in the supernova feedback momentum yield, according to differences in the galactic environments we have modeled, as noted by D. Martizzi et al. (2015) and C. C. Hayward & P. F. Hopkins (2017), among others.

We obtain a similar slope and normalization to that of the TIGRESS simulations, which are 1.21 and −7.66, respectively, and given by the dashed line in the figure. The slightly reduced normalization factor may be attributable to the different feedback model used in our simulations, or to the presence of radial mass transport, which is not present in stratified box simulations.

Excluding the dynamically suppressed galaxy, the correlation between $\Sigma_{\rm SFR}$ and $P_{\rm tot}$ in our simulations is tight, indicating that the midplane pressure is strongly correlated with the SFR, in line with theoretical expectations. We show explicitly in Appendix B and Figure 14 that the midplane pressure can be approximated by the ISM weight $\mathcal{W}$ across our simulation suite, given by

$$P_{\rm tot} \sim \mathcal{W} = \int_0^{z_{\rm max}} \rho_{\rm gas}(z)\frac{\partial\Phi}{\partial z}dz, \quad (7)$$

where $z_{\rm max}$ is the maximum extent of the gas disk, $\rho_{\rm gas}$ is the gas volume density, and Φ is the gravitational potential due to the entire distribution of gas, stars, and dark matter. The right panel of Figure 12 shows $\Sigma_{\rm SFR}$ versus $\mathcal{W}$, since $\mathcal{W}$ is more readily accessible in observations than a direct measure of $P_{\rm tot}$. The filled circles again represent measured values within annular radial bins, and gray crosses represent estimated values across the gas disks of the ATLAS$^{\rm 3D}$ sample, with a similar

[17] "Diffuse" is equivalent to the cold+warm, gravitationally unbound gas reservoir with $T \lesssim 10^4$ K and $\alpha_{\rm vir} > 2$. This gas accounts for the majority of the ISM by mass, and in our simulations we calculate $P_{\rm tot}$ for this cold+warm gas reservoir.

[18] In practice, J. Sun et al. (2023) calculate the ISM weight $\mathcal{W}$, as opposed to the pressure $P_{\rm tot}$, but we have placed the gray contours on the left panel of Figure 12 for visual clarity.

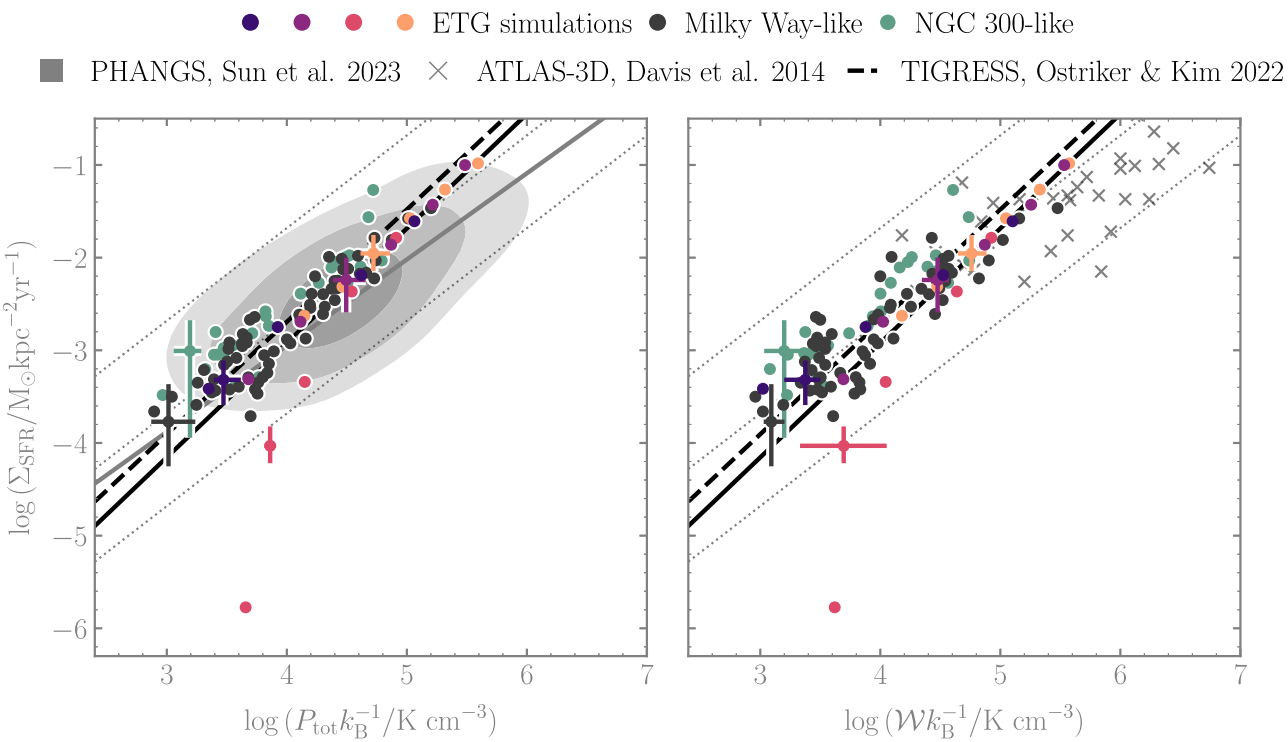

Figure 12. SFR surface density $\Sigma_{\rm SFR}$ as a function of the total midplane pressure $P_{\rm tot}$ (left) and as a function of the ISM weight $\mathcal{W}$ (right; see Section 5.2). Black dotted lines represent constant ratios of $\Sigma_{\rm SFR}/P_{\rm tot} = 10^2$, 10^3, and 10^4 km s^{-1}. Only the cool–warm gas ($T < 2 \times 10^4$ K) that is gravitationally unbound ($\alpha_{\rm vir} > 2$) is included in the calculation. Filled data points represent median values over time for each simulated galaxy, measured within overlapping radial annuli of width 500 pc. For visual clarity, the corresponding interquartile ranges are shown at just one representative radius in each galaxy. The thick black line represents the best linear regression fit to these data points, excluding the dynamically suppressed galaxy (pink). The thick dashed line represents the corresponding best fit from the TIGRESS simulations (E. C. Ostriker & C.-G. Kim 2022). The gray contours represent the 40%–80%–95% levels of the observed galaxy sample from J. Sun et al. (2023), and the gray crosses represent average values across the gas disks of the ATLAS$^{\rm 3D}$ galaxy sample from T. A. Davis et al. (2014), also shown in Figure 2. We note that J. Sun et al. (2023) strictly measure $\mathcal{W}$ to obtain $P_{\rm tot}$, but we include these data in the left panel for readability.

spread of $\Sigma_{\rm SFR}/P_{\rm tot}$ values. Our method for calculating $\mathcal{W}$ in both the simulations and observations is described in Appendix B.

It is worth noting that the ATLAS$^{\rm 3D}$ values of $\Sigma_{\rm SFR}/P_{\rm tot}$ in the right panel of Figure 12 display relatively good agreement with all four ETG simulations, including the dynamically suppressed galaxy simulation. That is, they extend to lower disk-averaged SFRs per unit ISM weight than do the spiral galaxies in the left panel of Figure 12. This finding is consistent with the suppression of the SFE in observed ETGs (e.g., T. A. Davis et al. 2014) by dynamical suppression (e.g., M. Martig et al. 2009; J. Gensior et al. 2020).

Figure 12 therefore demonstrates that, averaged over time, and with the exception of the dynamically suppressed galaxy, the gas disks of our simulated galaxies have $\Sigma_{\rm SFR}$ strongly correlated with $P_{\rm tot} \approx \mathcal{W}$. Because the ISM weight $\mathcal{W}$ can be calculated in terms of the large-scale properties of galaxies (see Section 3 of S. Hassan et al. 2024, for details), Equation (6) can therefore be used to model star formation in cosmological simulations, so long as the assumption of dynamical equilibrium holds and dynamical suppression of the SFE is not present.

In Figure 13, we show the same data as is presented in Figure 12, but in greater detail for each simulated galaxy, with interquartile ranges over time and azimuthal angle at each galactocentric radius (transparent shaded regions). The separate contributions to the ISM weight $\mathcal{W}$ made by the gas disk (solid lines), dark matter halo (dotted lines), stellar disk (dashed lines), and stellar bulge (thick dotted–dashed lines), at one single simulation time, are shown in the top row, clearly demonstrating that $\mathcal{W}$ is dominated by the stellar bulge in the ETG simulations, by the stellar disk in the Milky Way–like simulation, and by the disk and dark matter halo in the NGC 300–like simulation. We note that the strong dominance of the stellar disk weight contribution over the gas disk contribution in the Milky Way–like disk may not reflect the true balance of weights in the Milky Way, due to the small scale height of the stellar disk in the AGORA initial condition (∼100 pc), relative to the true value in the Milky Way (∼300 pc).

In the middle row of Figure 13, we show that a state of dynamical equilibrium is maintained across all of the galaxy simulations, with close overlap between the midplane pressure (thick solid lines) and the ISM weight (thick dashed lines). The thermal pressure (thin lines) is also shown, for comparison. The lack of an increase in $P_{\rm th}$ toward the inner parts of the Milky Way and NGC 300 models is likely due to the spatially and temporally constant radiation field we have adopted in our simulations. A more realistic model would have a radiation field that increases at higher $\Sigma_{\rm SFR}$ but would still produce a value of $P_{\rm th}$ that is subdominant to $P_{\rm turb}$ in all but very low weight environments (see E. C. Ostriker & C.-G. Kim 2022). Since $P_{\rm th} \ll P_{\rm turb}$ in the star-forming gas of the supersonic ISM, this should not affect the robustness of our results.

Finally, the bottom row of Figure 13 shows the correspondence between the measured SFR surface density $\Sigma_{\rm SFR}$ for each

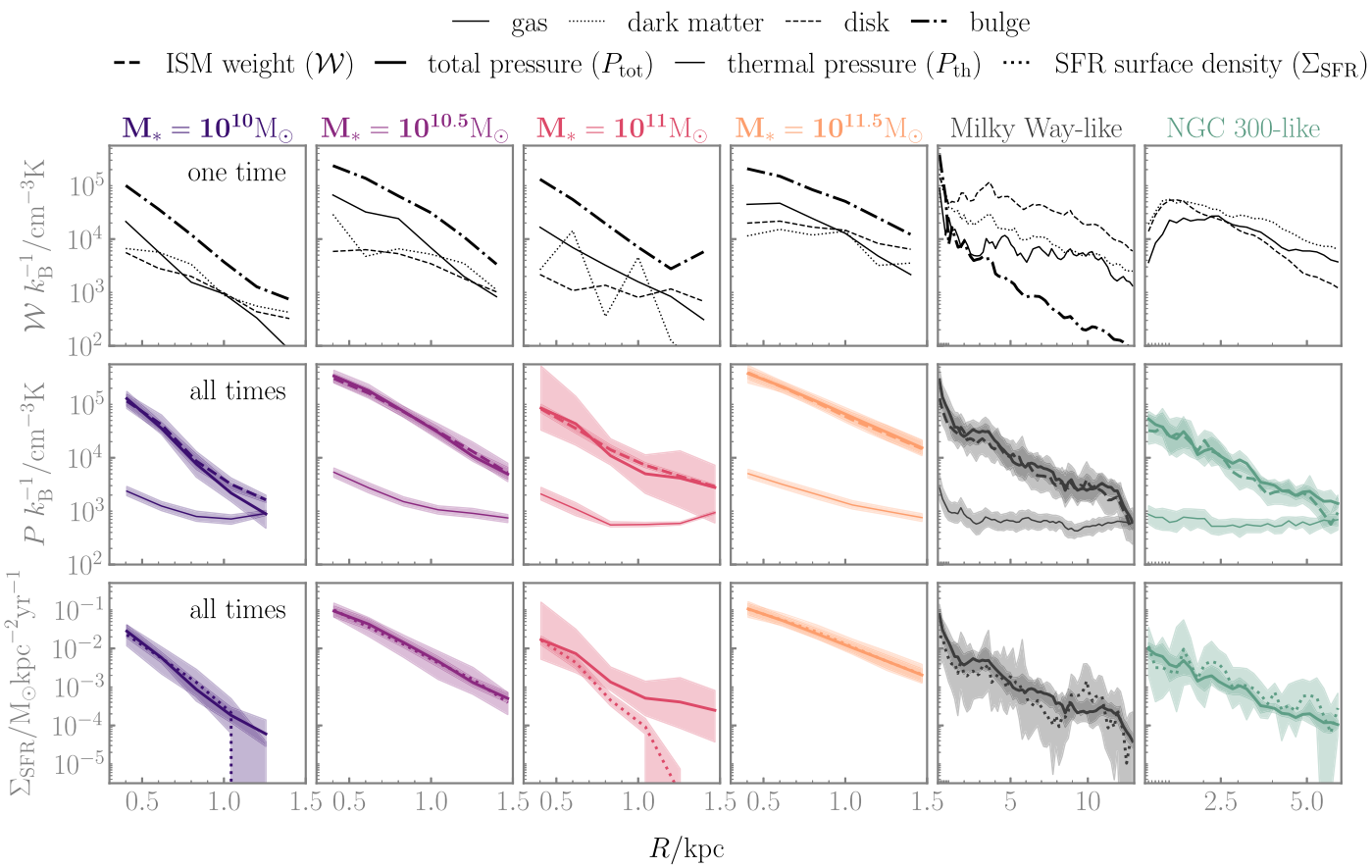

Figure 13. Top row: the ISM weight $\mathcal{W}$ due to each component of the gravitational potential, as a function of the galactocentric radius, at the final analyzed time of each simulation. Middle row: comparison of the total midplane pressure (solid lines) and the total ISM weight (dashed lines), along with median values of the thermal midplane pressure (thin lines) as a function of galactocentric radius. Only the cool–warm gas ($T < 2 \times 10^4$ K) that is gravitationally unbound ($\alpha_{\rm vir} > 2$) is included in the calculation of the pressures and SFRs. Bottom row: comparison of the true SFR surface density $\Sigma_{\rm SFR}$ (dotted lines) and the SFR surface density predicted by Equation (6). The bottom two rows are median values over time and azimuthal angle, and all shaded areas are the corresponding interquartile ranges.

simulation as a function of galactocentric radius and the value predicted via Equation (6). The same power-law relation between $P_{\rm tot}$ and $\Sigma_{\rm SFR}$ manifestly holds across five out of six galaxies, excluding the dynamically suppressed ETG.

We therefore find that Equation (6) holds promise as a predictive, first-principles subgrid model for star formation in cosmological simulations, across a range of star-forming main-sequence and bulge-dominated, quenched galaxy environments. This model provides an estimate for the SFR based on the theoretical prediction of E. C. Ostriker & C.-G. Kim (2022), rather than a fit to a relatively small sample of nearby main-sequence spirals, as is the current state of the art in cosmological simulations. It therefore has the potential to make reliable predictions of the SFR across a larger range of environments, particularly at high redshift.

By contrast, the SFR in the dynamically suppressed galaxy is decoupled from pressure regulation, as both the midplane turbulent pressure and galactic rotation appear to provide substantial support against gravitational collapse of the cold, star-forming gas. It is likely that the SFR in this galaxy is determined not just by the midplane gas pressure but also by the rate of galactic rotation. We will discuss this galaxy in detail in the second paper of this series, along with ways to incorporate the role of multiple physical mechanisms in driving (and thus predicting) the SFR.

6. Discussion and Summary

In this work we have presented six high-resolution chemodynamical simulations of galaxies spanning the dynamical environments of star-forming main-sequence and quenched (low-sSFR) galaxies, with a wide range of bulge-to-disk ratios, and hence a wide range of epicyclic frequencies. We have investigated their global properties: the regulation of star formation; the gas-phase distribution and the gas-phase morphology, related to the gravitational potential; the clustering of supernovae; and the driving of galactic outflows. We have found that varying the gravitational potential produces a large range of gas morphologies, phase structures, and SFRs, which are broadly in agreement with observations. We have quantified these variations with a view to modeling such environments in cosmological simulations. We can summarize our results as follows:

1. The level of supernova clustering, and thus the mass loading η of galactic outflows, is strongly coupled to the rate of galactic rotation κ, via the Toomre length scale for each disk. That is, higher rotation rates prevent large clusters from forming, such that star formation occurs in larger numbers of smaller clouds, which do not break out of the disk. The result is that the bulge-dominated galaxies have galactic outflows with mass loadings

reduced by four orders of magnitude, relative to the star-forming main-sequence galaxies.
2. The EOS (density vs. pressure) of the star-forming gas depends on its turbulent velocity dispersion and so also varies strongly with the level of supernova clustering and the rate of galactic rotation. The cold+warm gas reservoir in the ETGs has a higher density, lower velocity dispersion, and higher molecular gas fraction than in the main-sequence galaxies.
3. Aside from one dynamically suppressed ETG, with the highest epicyclic frequency κ, the midplane pressure is strongly associated with the SFR surface density $\Sigma_{\rm SFR}$ across both main-sequence and early-type environments, in agreement with E. C. Ostriker & R. Shetty (2011) and E. C. Ostriker & C.-G. Kim (2022). The relationship is tighter than that between $\Sigma_{\rm SFR}$ and gas surface density.

Our conclusions have important implications for the modeling of star formation and stellar feedback in cosmological simulations:

1. The relationship between the midplane gas pressure $P_{\rm tot}$ and the SFR surface density $\Sigma_{\rm SFR}$ represents an improved model for star formation across star-forming main-sequence and quenched galactic environments, relative to the Schmidt–Kennicutt relation.
2. Across galactic environments with widely varying levels of galactic rotation and epicyclic frequency κ, as seen across our GalactISM simulations, the EOS between the gas density and the pressure varies strongly with κ. The value of κ should therefore be taken into account when modeling the pressure of the star-forming gas (via the eEOS) and the mass loading of galactic outflows in cosmological simulations.
3. The onset of dynamical suppression introduces a transition away from pressure-regulated star formation, which depends nonlinearly on the rate of galactic rotation κ. This behavior represents the greatest challenge for parameterization in terms of galaxy properties that are resolved in cosmological simulations.

We are optimistic that, like the eEOS, the mass loading η of galactic outflows, and even the onset of dynamical suppression of the SFE, can be parameterized systematically in terms of large-scale galaxy properties such as the ISM weight $\mathcal{W}$ and κ. Across our galaxy sample, the variations in η, the degree of supernova clustering, and the SFE are not described by simple power laws. However, given a large number of high-resolution galaxy simulations across diverse galactic environments, from simulation suites such as GalactISM and TIGRESS, it might be possible to constrain these quantities via data-driven or machine learning techniques. An investigation of this possibility will in the future be enabled by the expertize in statistical modeling present in the Learning the Universe collaboration.

Acknowledgments

We thank an anonymous referee for the thorough and attentive reading of the paper, which improved the clarity of the text and conclusions. S.M.R.J. is supported by Harvard University through an Institute of Theory and Computation Fellowship. The work of E.C.O. and C.G.K. is supported by grant 10013948 from the Simons Foundation to Princeton University, sponsoring the Learning the Universe collaboration. J.G. gratefully acknowledges financial support from the Swiss National Science Foundation (grant no CRSII5_193826). G.L.B. acknowledges support from the NSF (AST-2108470, ACCESS), a NASA TCAN award, and the Simons Foundation. We thank Volker Springel for providing us access to Arepo, and we thank Mark Krumholz and Romain Teyssier for helpful discussions. We thank Jiayi Sun for the use of his script for plotting beautiful density contours for Figures 11 and 12.

Appendix A
Chemical Post-processing

As noted in Section 2.1, the CO-luminous gas fraction in our simulations is calculated in post-processing using the DESPOTIC model for astrochemistry and radiative transfer (M. R. Krumholz 2013). The self-shielding and dust shielding of CO molecules from the ambient UV radiation field cannot be accurately computed during run time at the mass resolution of our simulation. Within DESPOTIC, the escape probability formalism is applied to compute the CO line emission from each gas cell according to its hydrogen atom number density $n_{\rm H}$, column density $N_{\rm H}$, and virial parameter $\alpha_{\rm vir}$, assuming that the cells are approximately spherical. In practice, the line luminosity varies smoothly with the variables $n_{\rm H}$, $N_{\rm H}$, and $\alpha_{\rm vir}$. We therefore interpolate over a grid of precalculated models at regularly spaced logarithmic intervals in these variables to reduce computational cost. The hydrogen column density is estimated via the local approximation of C. Safranek-Shrader et al. (2017) as $N_{\rm H} = \lambda_{\rm J} n_{\rm H}$, where $\lambda_{\rm J} = (\pi c_s^2/G\rho)^{1/2}$ is the Jeans length, with an upper limit of $T = 40$ K on the gas cell temperature. The virial parameter is calculated from the turbulent velocity dispersion of each gas cell according to I. MacLaren et al. (1988) and F. Bertoldi & C. F. McKee (1992). The line emission is self-consistently coupled to the chemical and thermal evolution of the gas, including carbon and oxygen chemistry (M. Gong et al. 2017); gas heating by cosmic rays and the grain photoelectric effect; line cooling due to C^+, C, O, and CO; and thermal exchange between dust and gas. We match the ISRF strength and cosmic ionization rate to the values used in our live chemistry.

Having calculated values of the CO line luminosity for each simulated gas cell, we compute the CO-bright molecular hydrogen surface density as

$$\Sigma_{\rm H_2,CO}[M_\odot\ {\rm pc}^{-2}] = \frac{2.3\times10^{-29}\,M_\odot({\rm erg\ s^{-1}})^{-1}}{m_{\rm H}[M_\odot]} \times\int_{-\infty}^{\infty} dz' \rho_g(z') L_{\rm CO}[{\rm erg\ s^{-1}\ H\ atom^{-1}}], \quad \text{(A1)}$$

where $\rho_g(z)$ is the total gas volume density in $M_\odot\,{\rm pc}^{-3}$ at a distance z (in pc) from the galactic midplane. The factor of $2.3\times10^{-29}\,M_\odot\,({\rm erg\ s^{-1}})^{-1}$ combines the mass-to-luminosity conversion factor $\alpha_{\rm CO} = 4.3\,M_\odot\,{\rm pc}^{-2}({\rm K\ km\ s^{-1}})^{-1}$ of A. D. Bolatto et al. (2013) with the line luminosity conversion factor $5.31\times10^{-30}({\rm K\ km\ s^{-1}\ pc^2})/({\rm erg\ s^{-1}})$ for the CO $J = 1\rightarrow0$ transition at redshift $z = 0$ (P. M. Solomon & P. A. Vanden Bout 2005).

We note that our assumption of a constant H_2-to-CO conversion factor may introduce an overestimate of the CO-luminous molecular gas surface density at high gas surface densities. Additionally, for high column density regions in which the CO $J = 1$–0 line becomes optically thick,

Equation (A1) may overestimate the integrated emission for this particular line. Our CO-luminous molecular gas surface density is therefore necessarily an upper limit to the CO-luminous H_2 column.

We emphasize that this post-processing calculation of CO-bright H_2 emission is used only for the comparison of molecular half-mass radii and average surface densities in the creation of initial conditions to match the observational samples shown in Figure 2, for which Equation (A1) is sufficient. All other H_2 column densities are computed via the chemical network and shielding prescription outlined in Section 2.3, independently of the CO luminosity.

Appendix B
Calculation of Interstellar Medium Weights, Pressures, Velocity Dispersions, and Star Formation Rate Surface Densities

B.1. Values of Weight, Pressure, and Star Formation Rate from Simulated Data

In Figures 10, 12, and 13 we show the total midplane pressure $P_{\rm tot}$, the midplane volume density $n_{\rm H}$, and the gravitational weight $\mathcal{W}$ of the ISM across our simulation suite. These quantities are computed on a cylindrical three-dimensional grid in galactocentric radius R, azimuthal angle θ, and vertical distance z from the galactic midplane. The R-bins have a width of 500 pc and a separation of 200 pc, while the z-bins have a width of 10 pc and a separation of 10 pc. Twelve θ bins with $\theta \in [0, 2\pi]$ are used in every case.

In the calculation of all gas properties below, we exclude gas that is gravitationally bound with $\alpha_{\rm vir} < 2$ or that is in the hot, feedback-heated phase with $T > 2 \times 10^4$ K. That is, we include only the cool–warm gas phase; this gas is assumed to be in a state of vertical dynamical equilibrium in the theory of E. C. Ostriker et al. (2010) and E. C. Ostriker & C.-G. Kim (2022), and this equilibrium is directly demonstrated for a range of z within multiphase simulations in C.-G. Kim & E. C. Ostriker (2015), A. B. Gurvich et al. (2020), and A. Vijayan et al. (2020).

The ISM weight is computed over the set of gas cells within each (R, θ, z) bin, such that

$$\mathcal{W} = \left| \min \left[\sum_{z_{\Phi_{\rm min}}}^{z_{\rm max}} \rho(z) \frac{\partial \Phi}{\partial z}(z), \sum_{-z_{\rm max}}^{z_{\Phi_{\rm min}}} \rho(z) \frac{\partial \Phi}{\partial z}(z) \right] \right| \Delta z, \tag{B1}$$

where ρ is the gas volume density, $z_{\rm max} = 300$ pc for the ETG simulations, and $z_{\rm max} = 1.5$ kpc for the Milky Way–like and NGC 300–like simulations. The potential Φ in each bin is given by interpolating the gravitational potential values across the 150 particle centroids (stellar, dark matter, or gas particles of any phase) nearest to the center of the bin, using radial basis function interpolation (T. Hines 2023). The gradient $\partial\Phi/\partial z$ is then taken as the difference between adjacent bins along the z-axis.

In Equation (B1), the quantity $z_{\Phi_{\rm min}}$ represents the z-bin in each (R, ϕ) column for which $\rho\Phi$ is minimized. We treat this as the midplane of the gas disk. The minimum of the two sums on either side of $z_{\Phi_{\rm min}}$ then provides a measure of the compressive force per unit area that acts on the gas disk (the ISM weight). The difference in the absolute values of these sums provides a force per unit area that pushes the gas disk in one direction, rather than compressing it, and is therefore excluded.

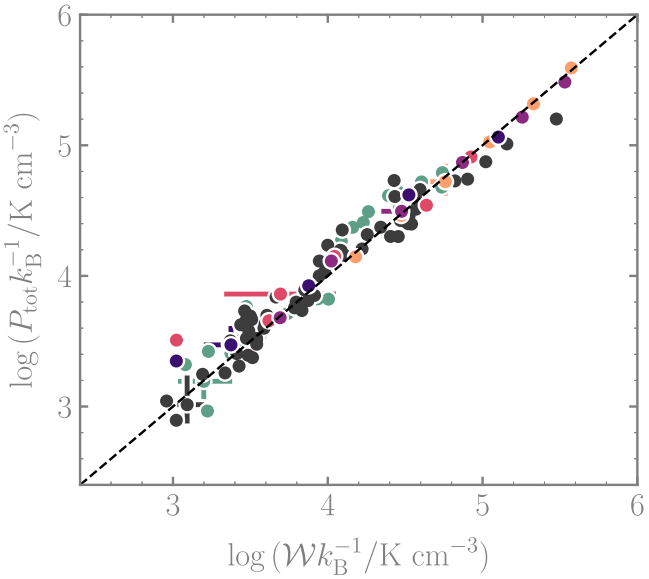

Figure 14. Total midplane gas pressure $P_{\rm tot}$ as a function of the ISM weight $\mathcal{W}$ for our six simulated galaxies. The dashed line represents the 1–1 relationship expected in dynamical equilibrium. Filled data points represent median values over time for each simulated galaxy, measured within overlapping radial annuli of width 500 pc. The Milky Way–like galaxy is represented by gray data points, the NGC 300–like galaxy by green data points, and the ETGs by the purple, pink, and orange data points. For visual clarity, the corresponding interquartile ranges are shown at just one representative radius in each galaxy.

Correspondingly, the volume-weighted midplane pressure is calculated for each column of (R, ϕ) at $z = z_{\Phi_{\rm min}}$, such that $P_{\rm tot} = P_{\rm th} + P_{\rm turb}$, with

$$P_{\rm th} = \rho c_s^2 |_{z = z_{\Phi_{\rm min}}} \tag{B2}$$

and

$$P_{\rm turb} = \rho (v_z - \langle v_z \rangle)^2 |_{z = z_{\Phi_{\rm min}}}. \tag{B3}$$

The volume density $\rho = n_{\rm H} \mu m_p$ of the gas cells is simply the sum of the gas cell masses divided by the bin volume (equivalent to a volume-weighted average of the gas cell densities). The angle brackets denote mass-weighted averages over each (R, ϕ) column (note that the volume-weighted pressure is given by the product of the volume-weighted gas density and the mass-weighted velocity dispersion, as shown explicitly in E. C. Ostriker et al. 2010). The gas velocity perpendicular to the galactic midplane is given by v_z, and c_s is the gas sound speed. Figure 13 shows that total midplane pressure does indeed balance the ISM disk's vertical weight in our simulations.

Finally, we calculate the SFR surface density $\Sigma_{\rm SFR}$ in each (R, ϕ) column by simply summing the instantaneous SFRs of the gas cells in each column and dividing by its surface area. We note that Figures 1 and 4, by contrast, use SFRs calculated as averages over star particles with ages $\leqslant$5 Myr, similar to the values that would be observed in Hα emission. We find good agreement between the the SFRs computed via these two methods.

The values of $\mathcal{W}$, $P_{\rm tot}$, and $\Sigma_{\rm SFR}$ shown in Figures 10–13 are median values over time and azimuthal angle. Because the turbulent velocity dispersion used to compute $P_{\rm turb}$ is a

statistical quantity (standard deviation of vertical velocities) and the SFR is computed stochastically for the gas cells in our simulation, we take medians and interquartile ranges only over the set of voxels with $\geqslant$100 gas cells.

Finally, we show explicitly in Figure 14 that the mid-plane pressure and the interstellar medium weight are linearly related across the three orders of magnitude spanned by our galaxies, consistent with the state of dynamical equilibrium discussed in Section 5.2 and implicitly demonstrated in Figures 10–13.

B.2. Calculation of the Radial Velocity Dispersions, σ_R and $\sigma_{R,*}$

In Figure 7, we show the radial component of the velocity dispersion for the gas and stellar components of the galactic disk, which provides support against the gravitational collapse of gas, as encapsulated in the Toomre Q parameter. We calculate these quantities as

$$\sigma_R^2 = \langle (v_R - \langle v_R \rangle)^2 \rangle$$
$$\sigma_{R,*}^2 = \langle (v_{R,*} - \langle v_{R,*} \rangle)^2 \rangle, \tag{B4}$$

where angle brackets again denote mass-weighted averages over the gas cells / stellar particles in each (R, ϕ) column.

B.3. Estimated Values for the ATLAS^{3D} Sample

In the right panel of Figure 12, we estimate the positions of the ATLAS^{3D} galaxies in the plane of ISM weight $\mathcal{W}$ versus the SFR surface density $\Sigma_{\rm SFR}$ (gray crosses). We have approximated $\mathcal{W}$ for the ATLAS^{3D} sample by making a number of geometrical approximations regarding the gas disk, stellar bulge, and dark matter halo. The median disk-to-bulge ratio in the galaxies is zero, such that

$$\mathcal{W} = \mathcal{W}_g + \mathcal{W}_{*,b} + \mathcal{W}_{\rm dm}, \tag{B5}$$

where $\mathcal{W}_g$ is the weight of the gas due to its own gravitational potential, $\mathcal{W}_{*,b}$ is the weight due to the potential associated with the stellar bulge, and $\mathcal{W}_{\rm dm}$ is the weight due to the potential associated with the dark matter halo. Assuming a plane-parallel geometry for the gas,

$$\mathcal{W}_g = \frac{\pi G \Sigma_g^2}{2}, \tag{B6}$$

where Σ_g is the gas surface density. Both the stellar bulge and dark matter components have spherical distributions, such that their combined weight can be approximated as

$$\mathcal{W}_{*,b} + \mathcal{W}_{\rm dm} = \zeta \Sigma_g (\Omega_{*,b}^2 + \Omega_{\rm dm}^2) h_g, \tag{B7}$$

where h_g is the gas disk scale height, and we have assumed that h_g is much smaller than the scale lengths of both the bulge and the halo, with $\zeta \sim 1/3$ (see E. C. Ostriker & R. Shetty 2011). For the ATLAS^{3D} galaxies, we assume a Plummer profile for the bulge and an NFW profile for the halo, as in our simulations, and calculate $\Omega_{*,b}$ and $\Omega_{\rm dm}$ from the measured values of the stellar half-light radius $R_{*,1/2}$ and the virial halo mass M_{200}, as shown in Figure 2. We set a gas disk scale height of $h_g = 25$ pc—the median scale height within our ETG simulations.

ORCID iDs

Sarah M. R. Jeffreson https://orcid.org/0000-0002-4232-0200
Eve C. Ostriker https://orcid.org/0000-0002-0509-9113
Chang-Goo Kim https://orcid.org/0000-0003-2896-3725
Jindra Gensior https://orcid.org/0000-0001-6119-9883
Greg L. Bryan https://orcid.org/0000-0003-2630-9228
Timothy A. Davis https://orcid.org/0000-0003-4932-9379
Lars Hernquist https://orcid.org/0000-0001-6950-1629
Sultan Hassan https://orcid.org/0000-0002-1050-7572

References

Agertz, O., Kravtsov, A. V., Leitner, S. N., & Gnedin, N. Y. 2013, ApJ, 770, 25
Benincasa, S. M., Wadsley, J., Couchman, H. M. P., & Keller, B. W. 2016, MNRAS, 462, 3053
Bertoldi, F., & McKee, C. F. 1992, ApJ, 395, 140
Bigiel, F., Leroy, A., Walter, F., et al. 2008, AJ, 136, 2846
Bigiel, F., Leroy, A. K., Walter, F., et al. 2011, ApJL, 730, L13
Bolatto, A. D., Wolfire, M., & Leroy, A. K. 2013, ARA&A, 51, 207
Cappellari, M., Emsellem, E., Krajnović, D., et al. 2011, MNRAS, 413, 813
Cappellari, M., Scott, N., Alatalo, K., et al. 2013, MNRAS, 432, 1709
Catinella, B., Saintonge, A., Janowiecki, S., et al. 2018, MNRAS, 476, 875
Chabrier, G. 2003, PASP, 115, 763
Chen, J., Bryan, G. L., & Salem, M. 2016, MNRAS, 460, 3335
Clark, P. C., Glover, S. C. O., & Klessen, R. S. 2012, MNRAS, 420, 745
Colombo, D., Sanchez, S. F., Bolatto, A. D., et al. 2020, A&A, 644, A97
Combes, F., Young, L. M., & Bureau, M. 2007, MNRAS, 377, 1795
da Silva, R. L., Fumagalli, M., & Krumholz, M. R. 2014, MNRAS, 444, 3275
Davé, R., Anglés-Alcázar, D., Narayanan, D., et al. 2019, MNRAS, 486, 2827
Davé, R., Thompson, R., & Hopkins, P. F. 2016, MNRAS, 462, 3265
Davis, T. A., Alatalo, K., Bureau, M., et al. 2013, MNRAS, 429, 534
Davis, T. A., Gensior, J., Bureau, M., et al. 2022, MNRAS, 512, 1522
Davis, T. A., Greene, J. E., Ma, C.-P., et al. 2019, MNRAS, 486, 1404
Davis, T. A., Young, L. M., Crocker, A. F., et al. 2014, MNRAS, 444, 3427
den Brok, J. S., Bigiel, F., Chastenet, J., et al. 2023, A&A, 676, A93
Donnari, M., Pillepich, A., Nelson, D., et al. 2019, MNRAS, 485, 4817
Donnari, M., Pillepich, A., Nelson, D., et al. 2021, MNRAS, 506, 4760
Dutton, A. A., & Macciò, A. V. 2014, MNRAS, 441, 3359
Elmegreen, B. G. 2011, ApJ, 737, 10
Fabian, A. C. 2012, ARA&A, 50, 455
Faucher-Giguère, C.-A., Quataert, E., & Hopkins, P. F. 2013, MNRAS, 433, 1970
Fielding, D., Quataert, E., & Martizzi, D. 2018, MNRAS, 481, 3325
Gallagher, M. J., Leroy, A. K., Bigiel, F., et al. 2018, ApJ, 858, 90
Gensior, J., Davis, T. A., Bureau, M., et al. 2023, MNRAS, 526, 5590
Gensior, J., & Kruijssen, J. M. D. 2021, MNRAS, 500, 2000
Gensior, J., Kruijssen, J. M. D., & Keller, B. W. 2020, MNRAS, 495, 199
Gentry, E. S., Krumholz, M. R., Dekel, A., & Madau, P. 2017, MNRAS, 465, 2471
Glover, S. C. O., & Clark, P. C. 2012, MNRAS, 421, 116
Glover, S. C. O., Federrath, C., Mac Low, M. M., & Klessen, R. S. 2010, MNRAS, 404, 2
Glover, S. C. O., & Mac Low, M.-M. 2007a, ApJ, 659, 1317
Glover, S. C. O., & Mac Low, M.-M. 2007b, ApJS, 169, 239
Goldbaum, N. J., Krumholz, M. R., & Forbes, J. C. 2015, ApJ, 814, 131
Gong, M., Ostriker, E. C., & Wolfire, M. G. 2017, ApJ, 843, 38
Grand, R. J. J., Gómez, F. A., Marinacci, F., et al. 2017, MNRAS, 467, 179
Grudić, M. Y., Hopkins, P. F., Faucher-Giguère, C.-A., et al. 2018, MNRAS, 475, 3511
Gurvich, A. B., Faucher-Giguère, C.-A., Richings, A. J., et al. 2020, MNRAS, 498, 3664
Habing, H. J. 1968, BAN, 19, 421
Hassan, S., Ostriker, E. C., Kim, C.-G., et al. 2024, ApJ, submitted
Hayward, C. C., & Hopkins, P. F. 2017, MNRAS, 465, 1682
Hernandez, X., Park, C., Cervantes-Sodi, B., & Choi, Y.-Y. 2007, MNRAS, 375, 163
Hernquist, L. 1990, ApJ, 356, 359
Hines, T. 2023, Python Package Containing Tools for Radial Basis Function (RBF) Applications, GitHub, https://github.com/treverhines/RBF
Hopkins, P. F., & Christiansen, J. L. 2013, ApJ, 776, 48
Hopkins, P. F., Quataert, E., & Murray, N. 2011, MNRAS, 417, 950

Hopkins, P. F., Wetzel, A., Kereš, D., et al. 2018, MNRAS, 480, 800
Indriolo, N., & McCall, B. J. 2012, ApJ, 745, 91
Jeffreson, S. M. R., Krumholz, M. R., Fujimoto, Y., et al. 2021, MNRAS, 505, 3470
Jeffreson, S. M. R., Semenov, V. A., & Krumholz, M. R. 2024, MNRAS, 527, 7093
Kennicutt, R. C., Jr 1998, ApJ, 498, 541
Kim, C.-G., Kim, J.-G., Gong, M., & Ostriker, E. C. 2023a, ApJ, 946, 3
Kim, C.-G., Kim, W.-T., & Ostriker, E. C. 2011, ApJ, 743, 25
Kim, C.-G., & Ostriker, E. C. 2015, ApJ, 815, 67
Kim, C.-G., & Ostriker, E. C. 2017, ApJ, 846, 133
Kim, C.-G., Ostriker, E. C., & Kim, W.-T. 2013, ApJ, 776, 1
Kim, C.-G., Ostriker, E. C., & Raileanu, R. 2017, ApJ, 834, 25
Kim, C.-G., Ostriker, E. C., Somerville, R. S., et al. 2020, ApJ, 900, 61
Kim, J.-G., Gong, M., Kim, C.-G., & Ostriker, E. C. 2023b, ApJS, 264, 10
Kim, J.-h., Abel, T., Agertz, O., et al. 2014, ApJS, 210, 14
Kim, W.-T., & Ostriker, E. C. 2001, ApJ, 559, 70
Kim, W.-T., Ostriker, E. C., & Stone, J. M. 2002, ApJ, 581, 1080
Koch, E. W., Rosolowsky, E. W., Lockman, F. J., et al. 2018, MNRAS, 479, 2505
Krajnović, D., Alatalo, K., Blitz, L., et al. 2013, MNRAS, 432, 1768
Kruijssen, J. M. D., Schruba, A., Chevance, M., et al. 2019, Natur, 569, 519
Krumholz, M., & Burkert, A. 2010, ApJ, 724, 895
Krumholz, M. R., 2013 DESPOTIC: Derive the Energetics and SPectra of Optically Thick Interstellar Clouds, Astrophysics Source Code Library, ascl:1304.007
Krumholz, M. R. 2014, MNRAS, 437, 1662
Krumholz, M. R., Burkhart, B., Forbes, J. C., & Crocker, R. M. 2018, MNRAS, 477, 2716
Krumholz, M. R., Fumagalli, M., da Silva, R. L., Rendahl, T., & Parra, J. 2015, MNRAS, 452, 1447
Krumholz, M. R., & Gnedin, N. Y. 2011, ApJ, 729, 36
Krumholz, M. R., & Matzner, C. D. 2009, ApJ, 703, 1352
Leroy, A. K., Schinnerer, E., Hughes, A., et al. 2021, ApJS, 257, 43
Liu, L., Bureau, M., Blitz, L., et al. 2021, MNRAS, 505, 4048
Lu, A., Haggard, D., Bureau, M., et al. 2024, MNRAS, submitted
Ma, C.-P., Greene, J. E., McConnell, N., et al. 2014, ApJ, 795, 158
MacLaren, I., Richardson, K. M., & Wolfendale, A. W. 1988, ApJ, 333, 821
Martig, M., Bournaud, F., Teyssier, R., & Dekel, A. 2009, ApJ, 707, 250
Martig, M., Crocker, A. F., Bournaud, F., et al. 2013, MNRAS, 432, 1914
Martizzi, D., Faucher-Giguère, C.-A., & Quataert, E. 2015, MNRAS, 450, 504
Mathis, J. S., Mezger, P. G., & Panagia, N. 1983, A&A, 500, 259
Matzner, C. D. 2002, ApJ, 566, 302
Murray, N., Quataert, E., & Thompson, T. A. 2010, ApJ, 709, 191
Murray, N., & Rahman, M. 2010, ApJ, 709, 424
Navarro, J. F., Frenk, C. S., & White, S. D. M. 1997, ApJ, 490, 493
Nelson, D., Pillepich, A., Springel, V., et al. 2018, MNRAS, 475, 624
Nelson, R. P., & Langer, W. D. 1997, ApJ, 482, 796
Orr, M. E., Fielding, D. B., Hayward, C. C., & Burkhart, B. 2022, ApJ, 932, 88
Ostriker, E. C., & Kim, C.-G. 2022, ApJ, 936, 137
Ostriker, E. C., McKee, C. F., & Leroy, A. K. 2010, ApJ, 721, 975
Ostriker, E. C., & Shetty, R. 2011, ApJ, 731, 41
O'Sullivan, E., Combes, F., Salomé, P., et al. 2018, A&A, 618, A126
Padoan, P., Haugbølle, T., Nordlund, Å., & Frimann, S. 2017, ApJ, 840, 48
Phillips, T. G., Ellison, B. N., Keene, J. B., et al. 1987, ApJL, 322, L73
Piotrowska, J. M., Bluck, A. F. L., Maiolino, R., & Peng, Y. 2022, MNRAS, 512, 1052
Plummer, H. C. 1911, MNRAS, 71, 460
Power, C., Navarro, J. F., Jenkins, A., et al. 2003, MNRAS, 338, 14
Romeo, A. B., Burkert, A., & Agertz, O. 2010, MNRAS, 407, 1223
Romeo, A. B., & Falstad, N. 2013, MNRAS, 433, 1389
Romeo, A. B., & Wiegert, J. 2011, MNRAS, 416, 1191
Russell, H. R., McNamara, B. R., Fabian, A. C., et al. 2016, MNRAS, 458, 3134
Russell, H. R., McNamara, B. R., Fabian, A. C., et al. 2019, MNRAS, 490, 3025
Safranek-Shrader, C., Krumholz, M. R., Kim, C.-G., et al. 2017, MNRAS, 465, 885
Saintonge, A., Catinella, B., Tacconi, L. J., et al. 2017, ApJS, 233, 22
Saintonge, A., Tacconi, L. J., Fabello, S., et al. 2012, ApJ, 758, 73
Salomé, P., & Combes, F. 2003, A&A, 412, 657
Schaye, J., Crain, R. A., Bower, R. G., et al. 2015, MNRAS, 446, 521
Smith, M. C., Bryan, G. L., Somerville, R. S., et al. 2021, MNRAS, 506, 3882
Smith, M. C., Fielding, D. B., Bryan, G. L., et al. 2024, MNRAS, 527, 1216
Sobolev, V. V. 1960, Moving Envelopes of Stars (Cambridge, MA: Harvard Univ. Press)
Solomon, P. M., & Vanden Bout, P. A. 2005, ARA&A, 43, 677
Springel, V. 2010, MNRAS, 401, 791
Springel, V., Di Matteo, T., & Hernquist, L. 2005, MNRAS, 361, 776
Springel, V., & Hernquist, L. 2003, MNRAS, 339, 289
Stone, J. M., & Gardiner, T. 2009, NewA, 14, 139
Stone, J. M., Gardiner, T. A., Teuben, P., Hawley, J. F., & Simon, J. B. 2008, ApJS, 178, 137
Sun, J., Leroy, A. K., Ostriker, E. C., et al. 2020, ApJ, 892, 148
Sun, J., Leroy, A. K., Ostriker, E. C., et al. 2023, ApJL, 945, L19
Tacconi, L. J., Genzel, R., Saintonge, A., et al. 2018, ApJ, 853, 179
Teng, Y.-H., Sandstrom, K. M., Sun, J., et al. 2023, ApJ, 950, 119
Thompson, T. A., Quataert, E., & Murray, N. 2005, ApJ, 630, 167
Utomo, D., Blitz, L., Davis, T., et al. 2015, ApJ, 803, 16
Veale, M., Ma, C.-P., Greene, J. E., et al. 2018, MNRAS, 473, 5446
Vijayan, A., Kim, C.-G., Armillotta, L., Ostriker, E. C., & Li, M. 2020, ApJ, 894, 12
Vogelsberger, M., Genel, S., Sijacki, D., et al. 2013, MNRAS, 436, 3031
Vogelsberger, M., Genel, S., Springel, V., et al. 2014, Natur, 509, 177
Welch, G. A., & Sage, L. J. 2003, ApJ, 584, 260
Westmeier, T., Braun, R., & Koribalski, B. S. 2011, MNRAS, 410, 2217
Wiklind, T., & Rydbeck, G. 1986, A&A, 164, L22
Williams, T. G., Bureau, M., Davis, T. A., et al. 2023, MNRAS, 525, 4270
Young, L. M., Bureau, M., Davis, T. A., et al. 2011, MNRAS, 414, 940